Sensing Interfacial Non-Faradaic and Faradaic Processes via Plasmonic-Enhanced Metallic Luminescence in Nano-Optoelectrodes

Yuming Zhao

Thesis submitted to the faculty of the Virginia Polytechnic Institute and State University in partial fulfillment of the requirements for the degree of

Master of Science

Electrical Engineering

Wei Zhou, Chair

Linbo Shao

Qiang Li

November 20th, 2023

Blacksburg, Virginia

Keywords: electrochemical surface-enhanced Raman spectroscopy (EC-SERS), nanoplasmonic metal luminescence, plasmon-enhanced electronic Raman scattering (PE-ERS), plasmon-enhanced vibrational Raman scattering (PE-VRS), interfacial science

Sensing Interfacial Non-Faradaic and Faradaic Processes via Plasmonic-Enhanced Metallic Luminescence in Nano-Optoelectrodes

Yuming Zhao

ABSTRACT

Metallic nanostructures supporting surface plasmon modes can concentrate optical fields, and enhance luminescence processes from the metal surface at plasmonic hotspots. Such nanoplasmonic metal luminescence contributes to the spectral background in surface-enhanced Raman spectroscopy (SERS) measurements and is helpful in bioimaging, nano-thermometry, and chemical reaction monitoring applications. Despite increasing interest in nanoplasmonic metal luminescence, little attention has been paid to investigating its dependence on voltage modulation. Also, the hyphenated electrochemical surface-enhanced Raman spectroscopy (EC-SERS) technique typically ignores voltage-dependent spectral background information associated with nanoplasmonic metal luminescence due to limited mechanistic understanding and poor measurement reproducibility. In this thesis, we combine the experimental observations and theoretical study on dynamic Faradaic & non-Faradaic modulated nanoplasmonic metallic luminescence and molecular vibrational Raman from hotspots at the electrode-electrolyte interfaces using multiple novel nano-optoelectrodes. Our work represents a critical step toward the general application of

nanoplasmonic metal luminescence signals in optical voltage biosensing, hybrid optical-electrical signal transduction, and interfacial electrochemical monitoring.

Sensing Interfacial Non-Faradaic and Faradaic Processes via Plasmonic-Enhanced Metallic Luminescence in Nano-Optoelectrodes

Yuming Zhao

GENERAL AUDIENCE ABSTRACT

Understanding the non-Faradaic and Faradaic process pathway is crucial for unraveling reaction mechanisms, developing efficient catalysts, designing bionsensing methodology, energy conversion and cellular stimulator [1-7]. Advances in spectroscopic techniques[8, 9] and computational models[3, 10] have facilitated the investigation of the non-Faradic and Faradaic processes. Unlike bulk reactions, interfacial electrochemical reactions occur in nanometer-thin layers[3, 11], necessitating highly sensitive detection methods. A significant challenge is background interference from bulk electrolytes and electrodes, often obscuring weak signals from the interfacial region – traditional spectroelectrochemistry struggles to match the high temporal resolution requirement due to noise [12, 13]. Surface plasmons have become a promising solution for enhancing the sensitivity of spectroelectrochemical techniques[14, 15]. Surface plasmons are collective oscillations of electrons at the metal-dielectric interface, which can focus and intensify optical fields at

the nanoscale[16], boosting diverse nonlinear emission signals, including fluorescence, Raman scattering, and harmonic generation[17-23]. By utilizing surface plasmons, spectroelectrochemistry techniques have shown promise in detecting interfacial activities with high sensitivity. In this thesis, we introduce a pioneering dual-channel *in situ* EC-SERS methodology, which is freewhich harnesses the synergy between plasmon-enhanced vibrational Raman scattering (PE-VRS) and plasmon-enhanced electronic Raman scattering (PE-ERS) interfacial signals to monitor and analyze the Faradaic and non-Faradaic process at the electrode-electrolyte interfaces.

Acknowledgements

Great thanks to my advisor- Dr. Wei Zhou and my group partners, who generously give me thorough assistance and advice not in academic but also in life. Appreciate to my family who have been giving me endless emotional support during all the years.

Chapter 1 Background & Introduction

Electrochemical surface enhanced Raman spectroscopy (EC-SERS)

It has been well studied that metal (such as gold and silver) nanostructures can support surface plasmonic polaritons (SPPs) which can concentrate light in visible and near infrared (NIR) wavelengths range near the metallic surface. Such effect which is called near fields enhancement can significantly enhance the optical processes ranging from metallic interband and intraband photoluminescence, molecular resonant and non-resonant Raman scattering and nonlinear harmonic generation[17-22, 24]. Generally, the components of SERS spectra can be divided into discrete plasmon-enhanced vibrational Raman scattering (PE-VRS) peaks which is generated from molecules at hotspots and broad continuous emission background which is generated from the metal plasmonic-enhanced luminescence[25, 26]. Specifically, surface-enhanced Raman spectroscopy (SERS) has received a lot of attention as its vibrational vibrational fingerprint specificity and plasmonic hotspot sensitivity[27]. These features make SERS a powerful tool to investigate electrochemical interfacial science which includes fields such as interfacial spectro-electrochemistry reaction analyses[28-30] and biochemical sensing[31-33]. To further integrate electrochemical voltage-current signals with spectral signals, the hyphenated technique called electrochemical surface-enhanced Raman spectroscopy (EC-SERS) is developed. . While several studies have shown a correlation between voltage and plasmon-enhanced metal luminescence within electrochemical setups[34-36],

a comprehensive understanding of the connection between electrode interfacial behavior and the microscopic representation of plasmon-enhanced metal luminescence remains elusive. Furthermore, most EC-SERS studies have employed nonuniform plasmonic devices based on metal nanoparticle aggregates or roughened metal electrodes with randomly distributed or mechanically unstable plasmonic hotspots[30-33, 37-39], limiting EC-SERS measurement reproducibility for reliable analysis of voltage-dependent spectral background information.

Chapter 2 Methodology

2.1 Design of plasmonic nano-optoelectrodes

In many biomedical and environmental applications using SERS/EC-SERS, it is highly desirable to employ near-infrared (NIR) laser excitation and Au-based plasmonic devices to (i) minimize molecular autofluorescence background, (ii) reduce cellular phototoxicity, (iii) ensure chemical stability and biocompatibility, and (iv) increase optical penetration depth in measurements. Therefore, we aim to design plasmonic nano-optoelectrodes with strong fields enhancement in the near infrared (NIR) wavelength range and good electrochemical conductivity.

To achieve the broadband fields enhancement in the NIR wavelength range, we have developed a universal design principle: With the multiple metal-insulator-metal (MIM) nanolaminate structure, broadband multiresoant plasmonic modes among visible-NIR wavelength range can be achieved.[40] Overall, the design flow is as follows: first via nanoimprinting or inverse-nanoimprinting techniques, we fabricate specific material (polymer, semiconductor or metallic materials) nanopillar or nanohole nanohole arrays with spatial periodicity. The aim of this step is to support the Bloch surface plasmons (SPs) and potential mode coupling to them. Next, by physics vapor deposition (PVD), we deposit multiple nanometer thick metal and dielectric material layers on the substrate. The aim of this step is to create multiple coupled plasmonic gap modes. The flow is illustrated in **Figure 2.1**.

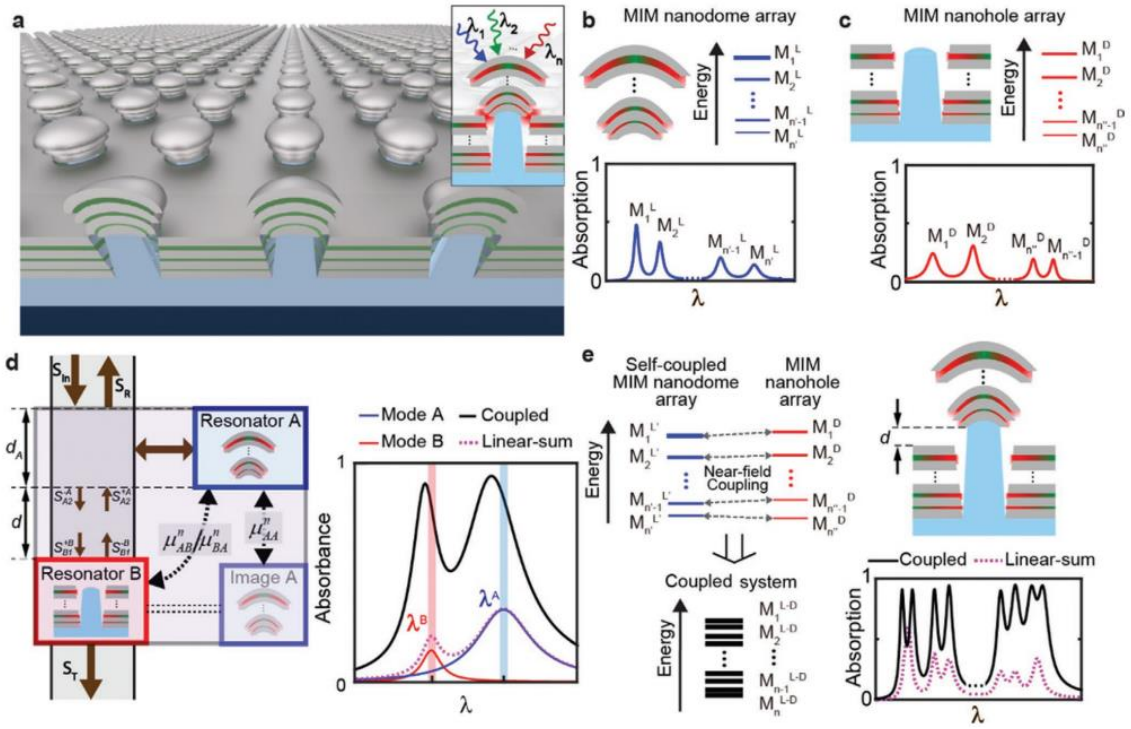

Figure 2.1 An overview of nanolaminate plasmonic substrates applying nanolaminate plasmonic modes coupling. Figures are originally from reference[40].

To verify that the optical properties of the designed substrate fulfill our needs before real fabrication process, we calculate the far-field and near-field optical response of the designed substrate using finite-difference time-domain (FDTD) method. The calculation is performed by the commercial software (Ansys Lumerical FDTD). **Figure 2.2** represents an example of the measured and calculated optical responses of one of our plasmonic nano-optoelectrode designs. Several statements can be made through the comparison between the measured the calculated results: First, generally the measured and simulated spectra agree in peak position despite the simulation produce narrower resonant features and the resonant peaks merge with each other to form broader resonant features in the measured spectra. This is due to the inhomogeneous broadening effect from geometric variations among periodic unit cells in the fabricated sample and the

homogeneous broadening effect from extra optical losses from nanostructure surface roughness[41]. Second, our design support strong field enhancements in the NIR wavelength ranges. From the simulated near fields maps, we notice that the locations with strong field enhancements, which are called hotspots, are mostly located at the pillar edges of the nanolaminate cavities. This is crucial for its further application in interfacial electrochemical analysis and biosensing.

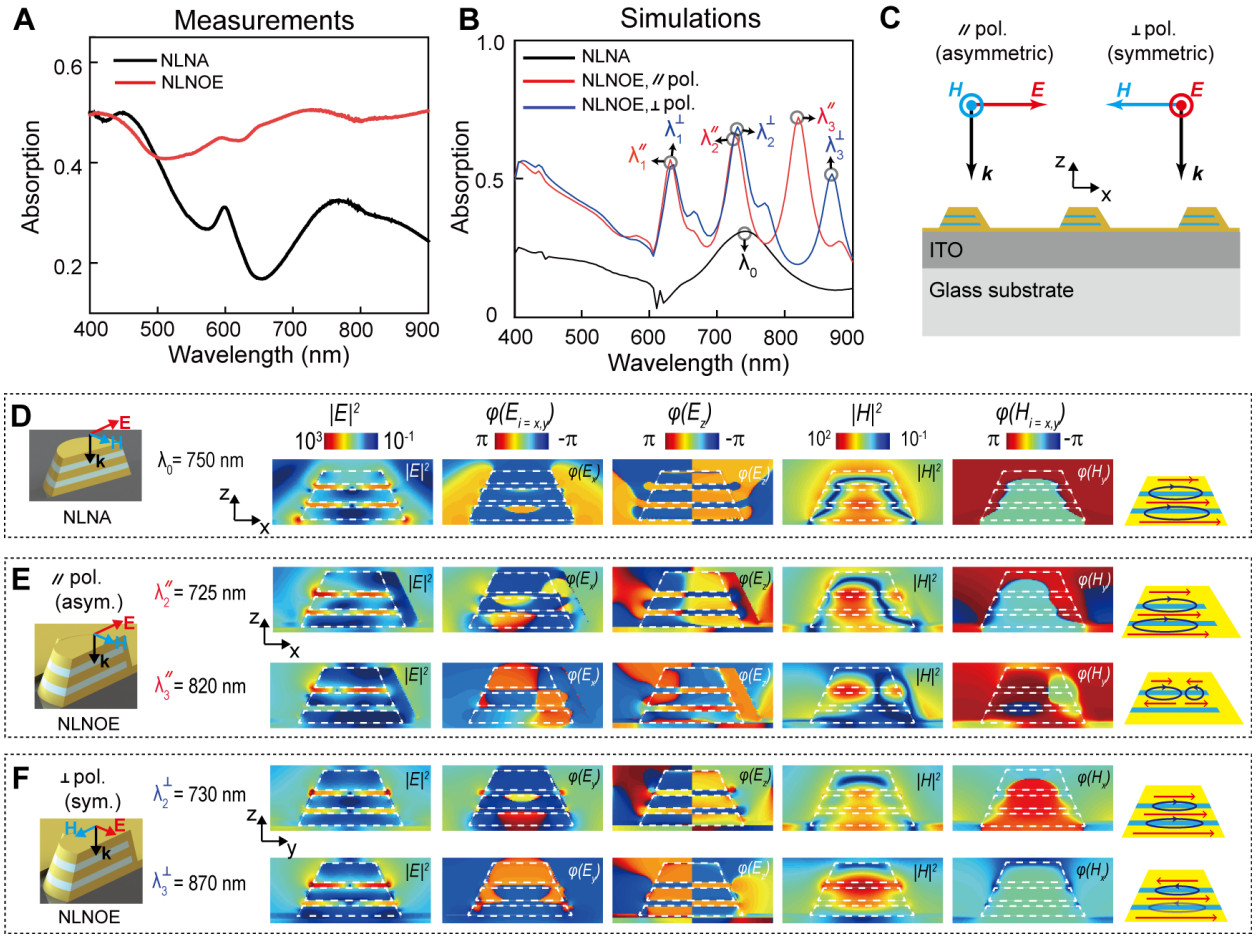

Figure 2.2 Example of optical characteristics of plasmonic nano-optoelectrode. [41] (A) Measured and (B) FDTD-calculated absorption spectra for substrate before (NLNA: nanolaminate nanoantenna) and after (NLNOE: nanolaminate nano-optoelectrode) post angled sidewall coating. (C) Light illumination scheme in FDTD simulations under different polarization excitation configurations regarding the mirror-symmetry x-z plane for NLNOEs. (D-F) FDTD-calculated near-field distribution maps at different wavelengths and excitation polarizations

To achieve good electrochemical conductivity, we develop two methodologies. The first is to use conductive materials to fabricate the nanopillar (or nanohole) array substrates beneath the metallic nanolayers. To introduce the conductivity, we mix the multiwall carbon nanotube (MWCNT) with polyurethane (PU) compound, which is an UV light curable polymer.[42] The second is to use a technique called post angled sidewall coating, which is, to our best knowledge, firstly developed by us[41]. Both methodologies will be introduced in more detail in the next section.

2.2 Fabrication of plasmonic nano-optoelectrodes

As mentioned in the previous section, we develop two designs of plasmonic nano-optoelectrodes with different methodologies to bring electrochemical conductivity.

2.2.1 Sample I: Two-tier Au/Ag/Au nanolaminate MWCNT doped nano-optoelectrode

First, a reusable inverse template of perfluoropolyether (PFPE) nanohole arrays on a polyethylene terephthalate (PET) substrate is used, derived from a silicon master of square pillar arrays via nanoimprint lithography. The PFPE template, with low surface energy and high Young's modulus, is ideal for molding a multiwall carbon nanotube (MWCNT, a mass fraction of 20 %) doped commercial UV light curable polyurethane (PU) compound, yielding conductive MWCNT/PU nanopillar arrays on Si substrates[42]. Subsequently, we deposited alternating Au ((≈25 nm) and Ag (≈8 nm, ≈10 nm, and ≈ 12 nm from bottom to top) thin films onto the nanopillar arrays via electron-beam evaporation, creating Au/Ag NLNOE arrays. A brief 1 min wet etching of Ag using Cr

etchant forms nanocavities for electrolyte penetration and increases sidewall roughness, exposing the hotspots at edges of nanocavities. The Sample I fabrication and result images are posted in **Figure 2.3 & 2.4**.

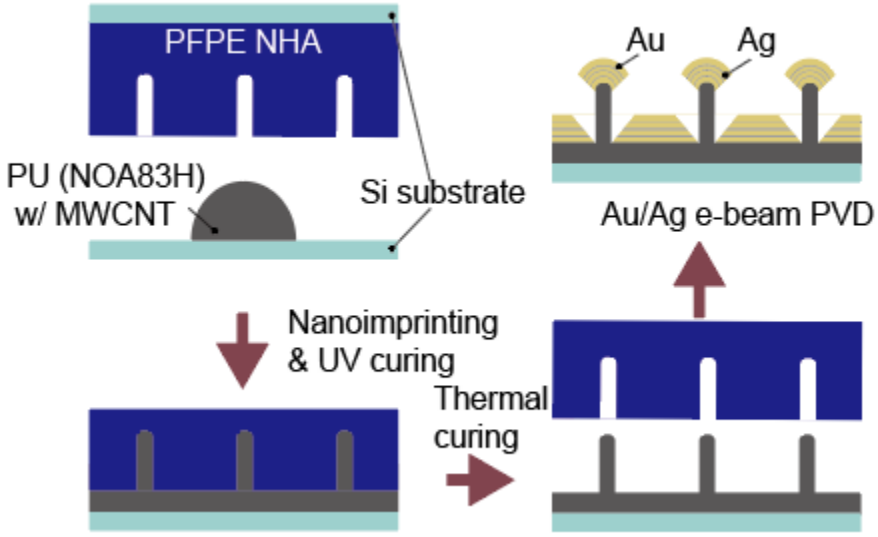

Figure 2.3 Schematic figure of Sample I fabrication

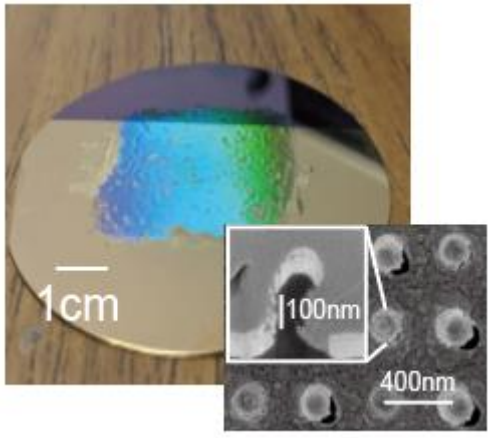

Figure 2.4 Optic and scanning electronic microscope (SEM) images of Sample I

2.2.1 Sample II: Au sidewall coating nanolaminate opto-electrode

First, a reusable PFPE nanopillar array template on a PET substrate was created from a silicon master of square nanowell (diameter ≈ 120 nm, depth ≈ 300 nm, and periodicity ≈ 400 nm) arrays using nanoimprint lithography. Next, the PFPE nanopillar array was spin-coated with diluted polymethyl methacrylate (PMMA) solution, and the PMMA nanowell arrays were transferred onto an ITO-coated glass slide using thermal nanoimprinting (~100 ℃, 12 hours). The PMMA nanowells were then transformed into nanoholes using

reactive-ion etching (RIE), forming a deposition mask for e-beam evaporation of alternating Au (≈25 nm) and SiO_2 (≈10 nm) thin-film layers. Subsequently, the PMMA was dissolved in anisole, removing excess material and revealing an array of nanoantenna with MIM nanocavities. Lastly, a ≈30 nm thick Au layer was coated on the nanoantenna with a tilted angle (≈50 °) for the substrate. The opto-electrode is achieved after the off-angle deposition of the Au layer. The Sample II fabrication and result images are posted in **Figure 2.5 & 2.6**.

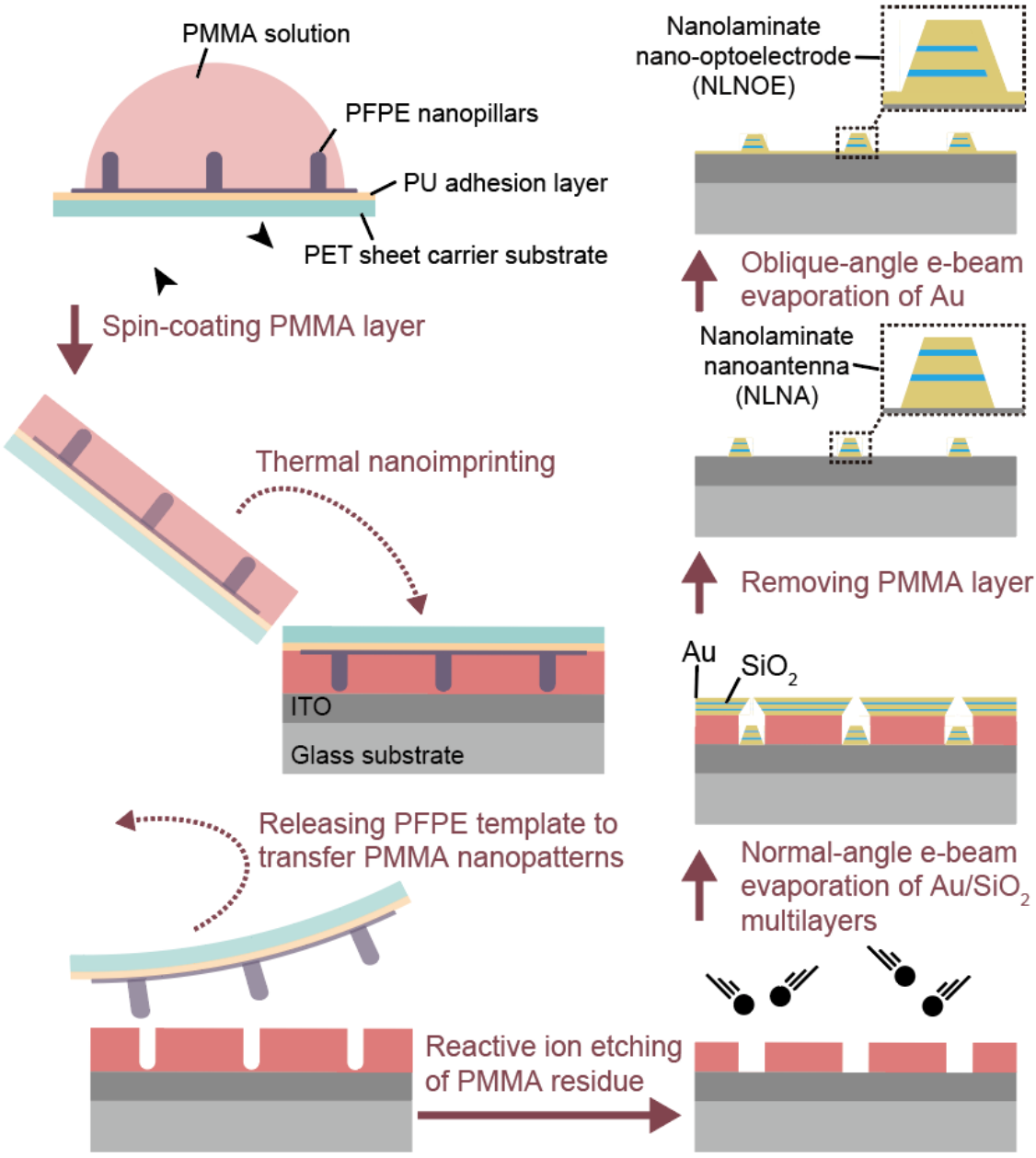

Figure 2.5 Schematic figure of Sample II fabrication

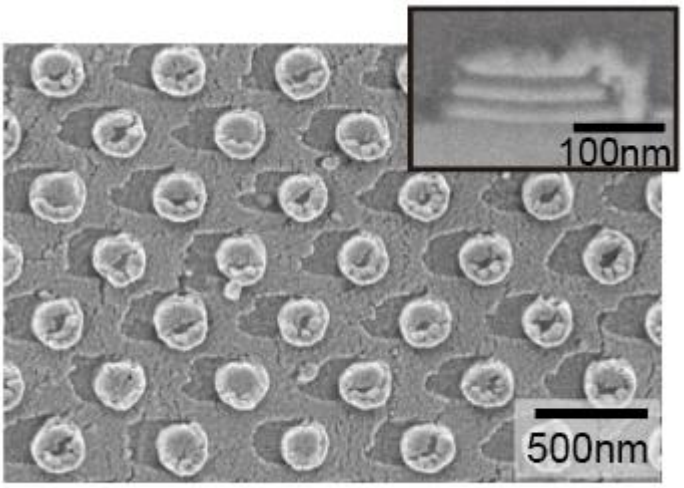

Figure 2.5 SEM images of Sample II

2.3 Characterization of nano-optoelectrodes

To evaluate the suitability of nano-optoelectrodes for *in situ* EC-SERS measurements, we systematically characterize their optical SERS enhancement factor and electrochemical conductivities:

To characterize the SERS enhancement factor, we compare the SERS spectra of the nano-optoelectrodes and flat gold samples with surface-modified benzenethiol (BZT) monolayers to the bulk neat BZT in ethanol solution. BZT is a universal Raman reporter to in the characterization of SERS enhancement factors. Both the nano-optoelectrode and flat gold sample is incubated in a 1 $mol \cdot m^{-3}$ BZT ethanol solution for 24 hours and then rinsed with ethanol. Both Raman signals were collected using a 20× objective (Numerical aperture = 0.4) with a 1 s integration time and ≈2 mW laser power. We calculated the SERS enhancement factors (EFs) of BZT molecules by formula: SERS EF = $(I_{SERS}/N_{SERS})/(I_{Raman}/N_{Raman})$, where I_{SERS}, I_{Raman}, N_{SERS}, and N_{Raman} are the BZT SERS intensity, neat BZT Raman intensity, and the number of BZT molecules contributing to BZT SERS and neat BZT

Raman intensities, respectively. N_{SERS} was calculated by the formula $N_{SERS} = S \times \sigma_{SERS}$, where S is the total exposed surface area of nano-optoelectrode layer within the $1\mu m^2$ laser beam spot area and σ_{SERS} is the BZT's surface packing density on the metal surface [(3.3×10^{14}) cm^{-2}] [43, 44]. N_{Raman} is calculated by $N_{Raman}=A\times d_{eff}\times \rho BZT$, where A is the laser beam spot area, d_{eff} is the effective depth of the laser beam spot under 20× objective, and ρ_{BZT} is the neat BZT molecule density [(5.9×10^{21}) cm^{-3}]. For I_{SERS} and I_{Raman}, we selected 1082 cm^{-1} Raman peak's intensity to calculate the SERS EF, which corresponded to the C–C–C ring in-plane breathing mode of BZT molecules[45]. **Figure 2.6** displays the comparative analysis of averaged spectra of BZT on planar gold and nano-optoelectrode (Sample I) from area scans. Flat gold samples lack discernible BZT peaks, whereas the nano-optoelectrode significantly enhances BZT signature peaks due to plasmon enhancement. We estimated the SERS EFs of NLNOEs to be $\approx 10^6$ under 785 nm laser excitation using the formula we just mention: SERS EF = $(I_{SERS}/N_{SERS})/(I_{Raman}/N_{Raman})$. Therefore, the nano-optoelectrode we fabricate is capable of in-situ EC-SERS measurements with high temporal resolution.

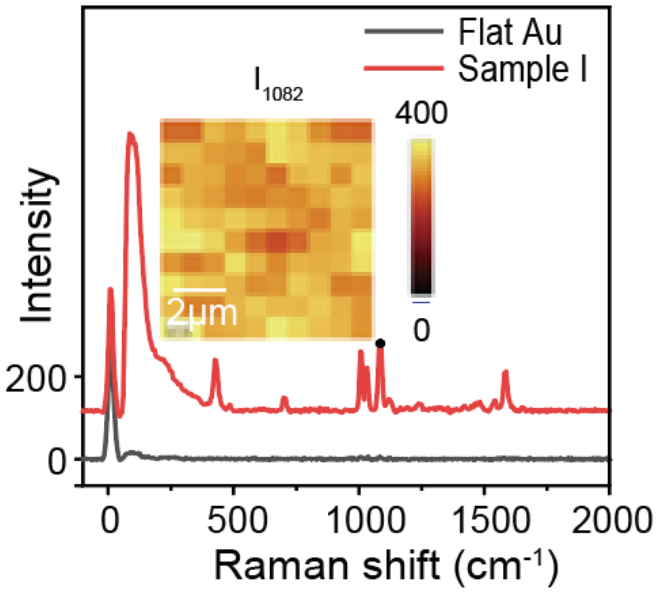

Figure 2.6 SERS enhancement factor (EF) characterization using benzenethiol (BZT) molecules for nano-optoelectrode sample I and flat gold.

To examine the electrical and electrochemical properties of the nano-optoelectrode at the electrode/electrolyte interface, we conducted electrochemical impedance spectroscopy (EIS) on optoelectrode submerged in a 1× Phosphate-Buffered Saline (PBS) solution (pH=7.4), maintained at ambient temperature. The EIS measurement is performed by a commercial potentialstat (SP-200, BioLogic) with the frequency ranging from 1 to 10^5 Hz. Then we apply the commercial software integrated with the device (EC-lab, BioLogic) to perform the EIS impedance fit. The resultant Nyquist plot and the curve fitted via the equivalent circuit are depicted in **Figure 2.7**, where the R and C represents for resistance and capacitance elements, respectively; $Q_2(f) = \frac{1}{q_2(i2\pi f)^{a_2}}$ is the constant phase element (CPE) which reflects the porous nature of the nanocavities as the charges near the electrode do not distribute as ideal electrical double layer (EDL). For an ideal EDL electrode, the CPE will turn out to be an ideal

capacitor, in which the index a=1. For our nano-optoelectrode, a=0.745 which is smaller than 1, indicating the fractional ions diffusion with nanostructure geometric constraints near the electrode [46]. $W_2(f) = \sqrt{\frac{s_2^2}{i\pi f}}$ is the Warburg impedance, which models semi-infinite linear diffusion. It turns out to be a good agreement with the measured data and all the fitted parameters are shown in the following **Table 2.1**. Overall, the EIS measurements show the good electrochemical conductivity of nano-optoelectrodes

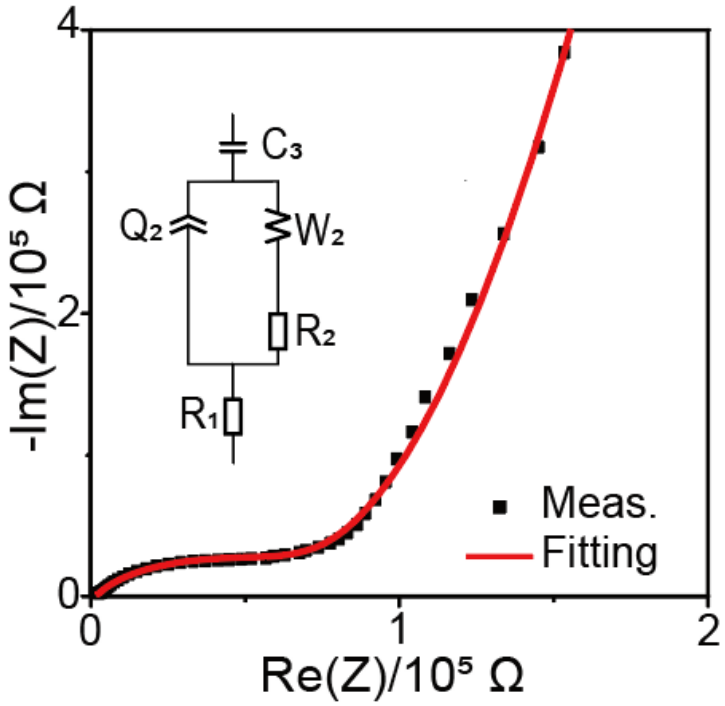

Figure 2.7 Electrochemical impedance spectroscopy (EIS) of nano-optoelectrode (Sample I) and the corresponding equivalent circuit with parameters obtained from fitting.

	value	unit	deviation
R_1	1875	Ω	0.4665
q_2	2.43×10^{-8}	$F \cdot s^{(a_2-1)}$	8.00×10^{-12}
a_2	0.7451		0.5
R_2	68170	Ω	2.692
s_2	351367	$\Omega \cdot s^{(-1/2)}$	10.1
C_3	2.20×10^{-7}	F	1.33×10^{-12}

Table 2.1. Parameters of EIS equivalent circuit impedance fit

2.4 Set-up of in-situ EC-SERS

A custom-made EC cell is constructed to contain the liquid and mounted onto the sample. An Ag/AgCl electrode saturated in KCl served as the reference electrode, while a platinum coil functioned as the counter electrode. Phosphate buffer saline (PBS) is employed as the electrolyte solution, consisting of 137 mM NaCl, 2.7 mM KCl, 10 mM Na_2HPO_4, and 1.8 mM KH_2PO_4. Deionized water is used for the dilution of the PBS. Approximately 2 mL of the electrolyte solution is introduced into the EC cell, and measurements are conducted at room temperature. To prevent electrolyte purging issues over an extended time scale (hours), we carry out all measurements within approximately 10 minutes immediately following the addition of the liquid. For all measurements, the substrate is rinsed with the corresponding concentration of PBS solution between each use to ensure cleanliness and reliability. Raman measurements are done under laser excitation at a wavelength of 785 nm and power of 2mW via a 10× objective (NA = 0.25) lens with a commercial confocal microscope in the backscattering configuration. Single-

point measurements were done at a 0.5 s integration time and acquired by a CCD camera in a commercial spectrometer to measure the Stokes-Raman scattering. A long-pass filter is used to block elastically scattered light at the wavelength corresponding to the laser line (Rayleigh scattering), and the Stokes scattering passed through a multimode fiber (100 µm core diameter) with the cleaved fiber core acting as the confocal pinhole. The electrochemical modulation is done using a custom EC cell and commercial potentiostat with the nano-optoelectrode as the working electrode, platinum coil as the counter electrode, and Ag/AgCl as the reference electrode. The schematic figure of the EC-SERS set-up and measurement are depicted in **Figure 2.8&2.9**.

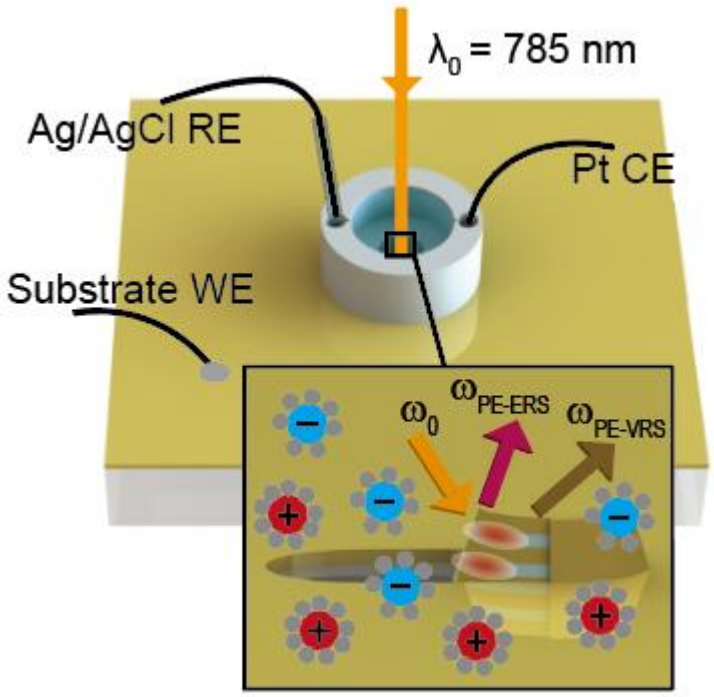

Figure 2.8 Schematic figure of EC-SERS set-up. WE, CE and RE stand for working, counter and reference electrode

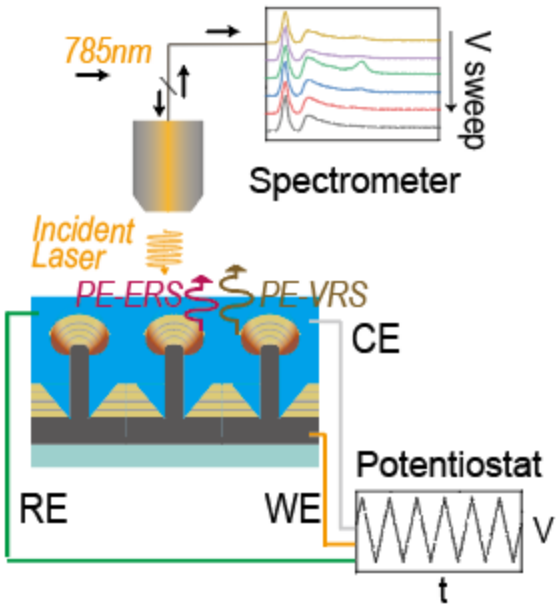

Figure 2.9 Schematic figure of EC-SERS measurement. The schematic of sample stands for nano-optoelectrode sample I.

2.5 Components of SERS spectrum: plasmonic enhanced electronic Raman scattering (PE-ERS) & plasmonic enhanced vibrational Raman scattering (PE-VRS)

As we have mentioned, the SERS spectrum are composed of the continuous background and discrete vibrational Raman related peaks. Although there is still debate, recent studies[47-49] have revealed that PE-ERS primarily accounts for the low-wavenumber background in SERS measurements from noble metal nanocavity hotspots under continuous wavelength (CW) laser excitation at near-infrared (NIR) wavelengths, as the interband transitions[50, 51] do not occur by low photon energy, and intraband transitions [52, 53] are unlikely due to momentum mismatch from sp-band dispersion. PE-ERS in metal originates from the electron-hole pair transitions near the Fermi energy E_F (**Figure 2.10-A**), with intensity proportional to $n_{e-h}(\Delta\omega) \propto n(E_F)\left|\exp\left(-\frac{\hbar\Delta\omega}{k_B T}\right)-1\right|^{-1}$, where $n(E_F)$

denotes the free electron density and $\left|\exp\left(-\frac{\hbar\Delta\omega}{k_B T}\right)-1\right|^{-1}$ is the Bose-Einstein distribution of the electron-hole pairs at Raman-shift frequency $\Delta\omega$. Utilizing a long-pass filter to eliminate elastic laser scattering, we obtain a PE-ERS pseudo peak in the spectra (**Figure 2.10-A**, **bottom**)[48]. In contrast to the continuous nature of PE-ERS signals, PE-VRS signals exhibit discrete peaks due to inelastic scattering involving distinct molecular vibrational modes (**Figure 2.10-B**). Both ERS and VRS signals undergo enhancement by a factor of $|\boldsymbol{E_{SP}}|^4/|\boldsymbol{E_0}|^4$ in plasmonic nanocavity hotspots, , where $\boldsymbol{E_{SP}}$ is the local plasmonic electrical field and $\boldsymbol{E_0}$ is the electrical field of incident excitation light[47].

During *in situ* EC-SERS measurements PE-ERS and PE-VRS signals, originating from electronic states and molecular vibrational bonds at electrode/electrolyte interfaces, respectively, within the plasmonic hotspots can provide complementary insights into interfacial electrochemical activities during redox reactions.

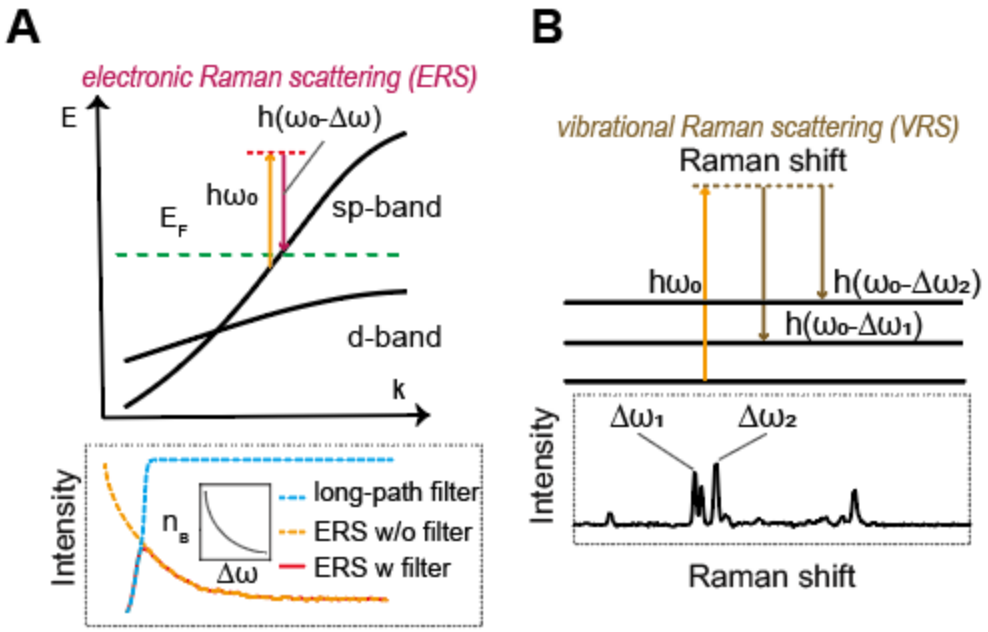

Figure 2.10 Schematic figure of (A) electronic Raman scattering (ERS) & (B) vibrational Raman scattering (VRS)

Chapter 3 Measurement Results

3.1 In-situ EC-SERS measurement on nano-optoelectrode Sample I: monitoring & analysis on Faradaic process

To confine and control redox reaction at the Ag nanogap cavities in nano-optoelectrode Sample I, we conduct cyclic voltammetry within a potential window of 0.4 V to 0.6 V at a low scan rate of 50 mV/s to induce the $AgCl(s) + e^- \rightleftharpoons Ag(s) + Cl^-(aq)$ redox reaction, while the Au layer remains unreactive[54]. As shown in the upper segment of **Figure 3.1-A**, cyclic voltage sweeps result in periodic current modulations, a behavior indicative of the reversible nature of Faradaic and non-Faradaic processes on stable NLNOEs.

The lower segment of **Figure 3.1-A** displays time-resolved two dimensional EC-SERS maps, spanning from -50 cm^{-1} to 1500 cm^{-1} across six cycles. To pinpoint the spectral features more precisely during the redox reaction, we selected 2×6 spectra (range -50 cm^{-1} to 500 cm^{-1}) from a single redox cycle (100 s to 140 s, the 3rd cycle), as shown in **Figure 3.1-B**. These measured spectra unveil three key characteristics: Firstly, the elastic scattering peak at 0 cm^{-1} remains relatively consistent during the redox reaction; secondly, both the PE-ERS pseudo-peak at ≈87 cm^{-1} and the PE-VRS peak at ≈ 258 cm^{-1} for the Ag-Cl bonds[55, 56] undergo substantial modulation at ±0.2 V during oxidation and reduction, respectively; and thirdly, PE-VRS experiences a more significant increase in peak intensity at 0.2V during oxidation compared to -0.2 V during reduction. **Figure 3.1-C** shows the nuanced relationship between electrochemical modulations and alterations in

several distinct EC-SERS spectral features. Specifically, we inspect the interdependencies between electrochemical current *I* and the normalized emission intensities of PE-VRS, PE-ERS, and elastic scattering signals during voltage modulations from a single (3rd) cycle.

The measurements reveal several notable observations. Firstly, well-defined Faradaic peaks, marked by an oxidation peak at ≈0.38 V and a reduction peak at ≈-0.22 V, become visible during voltage sweeps, indicative of the $AgCl(s) + e^- \rightleftharpoons Ag(s) + Cl^-(aq)$ redox reaction[54]. The ≈0.6 V redox peak-to-peak distance is considerably larger than that of ordinary Ag/AgCl cyclic voltammetry under similar conditions (≈0.152V)[57], implying that the redox reaction has a quasi-reversible behavior[11]. A probable explanation for the low electron transfer rate of the reaction is the formation of nanoporous electrolyte networks within Ag/AgCl matrices inside the Au-Ag-Au nanocavities during redox reactions, which limits the mass transport of ions involved in reactions and thereby impedes the reaction rate[56]. Secondly, we observe a PE-VRS peak at ≈258 cm^{-1}, linked to the stretching vibration of Ag-Cl bonds[55, 56]. The intensity of this peak during voltage modulation exhibits unsynchronized behavior in the Faradaic region for reduction or oxidation, with the PE-VRS peak intensity voltage preceding the Faradaic current peak voltage. We suggest that this PE-VRS peak relates to the (AgCl)* TS, having partial bonding with increased ability for its electron cloud distortion and enhanced polarizability changes compared to the steady-state Ag-Cl bond with a polar covalent nature, resulting in an increased VRS transition dipole moment and

amplified PE-VRS signals only during the redox reaction. This observation suggests that the opposing electrical field directions between reduction and oxidation cycles alter the microscopic VRS dipole moment orientation for (AgCl)* relative to the plasmonic electric field, resulting in varying PE-VRS emission intensities. In the non-Faradaic region, PE-VRS peak intensity increases linearly with voltage due to non-Faradaic capacitive modulation of metal surface charges at hotspots, consistent with our earlier study[58]. Thirdly, the PE-ERS pseudo peak at ≈87 cm^{-1} and tail intensities from 400 to 1400 cm^{-1} exhibit similar voltage-dependent behavior, indicating a common origin. Additionally, the PE-VRS peak at ≈258 cm^{-1} and the PE-ERS pseudo peak at ≈87 cm^{-1} display identical voltage conditions for their peaks, dips, turn-on, and turn-off transitions, revealing a strong link between PE-VRS and PE-ERS events due to the generation of (AgCl)* TS in redox reactions. Notably, PE-ERS intensity changes are consistent in positive and negative voltage sweeps under Faradaic modulation, suggesting that varying electrical field directions during reduction and oxidation cycles do not impact the ERS dipole moment orientation for (AgCl)* relative to the plasmonic field. Finally, in contrast to redox-modulated PE-VRS and PE-ERS, the inelastic scattering peak at 0 cm^{-1} shows minor random fluctuations (≈10%), which is possibly due to plasmonic heating causing local refractive index changes from local temperature fluctuation[59] or vapor/gas bubble formation[60], consequently altering the optical path and efficiency of elastic scattering signal collection.

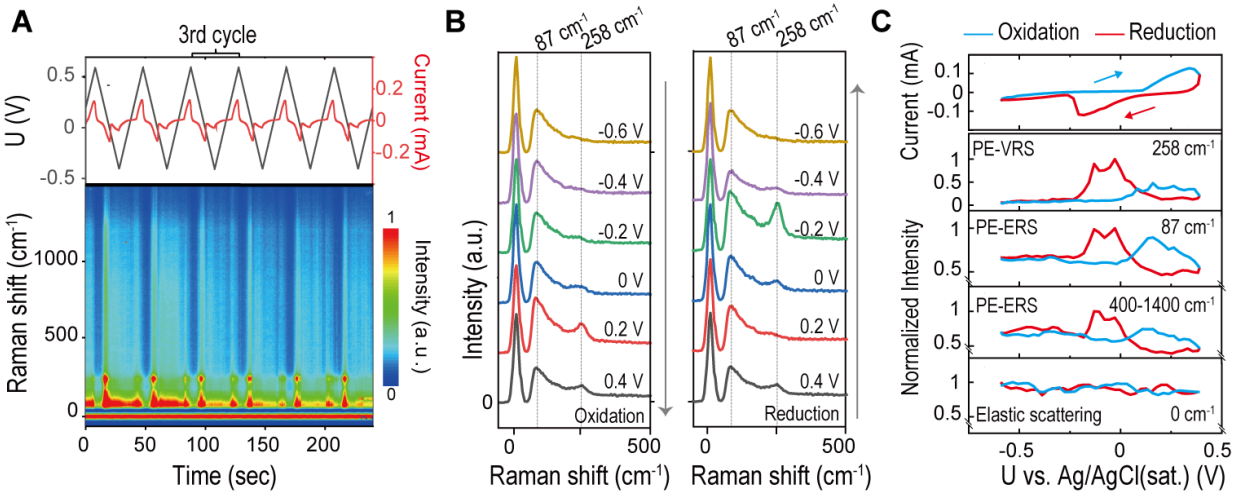

Figure 3.1 EC-SERS measurements of PE-ERS and PE-VRS signals from nano-optoelectrode Sample I under electrode potential modulation during $AgCl(s) + e^- \rightleftharpoons Ag(s) + Cl^-(aq)$ redox cycles. (A) Temporal current measurements (top) during cyclic voltammetry from -0.4 to 0.6 V, and time-resolved EC-SERS spectra (bottom) under 785 nm laser excitation using Sample I in 1× PBS solution. (B) EC-SERS emission spectra from Sample I in 1× PBS under 785 nm laser excitation at potentials ranging from -0.4 to 0.6 V during one redox cycle, showcasing oxidation (left) and reduction (right) phases. (C) Cyclic potential-dependent current (top) and normalized EC-SERS emission intensities (bottom) for PE-VRS peak at 258 cm-1 linked to stretching vibration of Ag-Cl bonds, PE-ERS pseudo-peak at 87 cm-1, PE-ERS broad continuum intensity integrated from 400 cm-1 to 1400 cm-1, and elastic scattering peak at 0 cm-1.

3.2 In-situ EC-SERS measurement on nano-optoelectrode Sample II: monitoring & analysis on nonFaradaic process

To investigate the effects of electrode potential modulation on PE-ERS and PE-VRS signals, we perform in situ EC-SERS measurements of the nano-optoelectrode sample I as the WE in 1×phosphate-buffered saline (PBS), using cyclic voltage sweep between –0.5 V and 0.5 V at a voltage sweep rate of 50 mV/s with a saturated Ag/AgCl reference electrode. As shown in **Figure 3A-top**, the cyclic voltage sweep causes the periodic current modulations within ± 0.2 mA associated with reversible non-Faradaic capacitive charging-discharging processes at the NLNOE surface[61]. The redox reaction between Au atoms and Cl^- ions at the electrode surface typically requires a higher positive potential (>1.5 V *vs.* AgCl/Cl)[11]. **Figure 3A-bottom** shows the time-dependent *in situ* EC-SERS spectra from –50 cm^{-1} to 500 cm^{-1}, where the dominant feature at ≈87 cm^{-1} is periodically modulated under cyclic voltage sweeping. **Figure 3B** illustrates five EC-SERS spectra recorded between –0.5 V and 0.5 V in a half-cycle with several key observations. First, the small peak at ≈0 cm^{-1} accounts for the elastic scattering signal from the excitation laser (785 nm) leaking through the long-pass filter. Second, the asymmetric voltage-dependent spectral feature at ≈87 cm^{-1} is a PE-ERS pseudo-peak due to the long-pass filter modification of the continuous Stokes ERS emission associated with the Bose-Einstein distribution of the metal sp-band electron-hole pairs at Stokes-shifted frequency $\Delta\omega$[25, 49, 62], which decreases with the applied potential. Third, a PE-VRS shoulder feature at ≈270 cm^{-1} on top of the PE-ERS spectral background is from Au-Cl bonds formed on

the gold surface[63, 64], which increases with the applied potential because of the attraction of the Cl- ions to the gold surface under a positive potential.

Figure 3C compares the measured electrode potential dependence of the charging-discharging current and the emission modulation ratios (ΔI/I) for PE-ERS, PE-VRS, and elastic scattering signals in a single cycle. First, by modeling the dominant non-Faradaic capacitive interfacial process with an equivalent circuit[65] consisting of a double-layer capacitor (C) and an ohmic resistance (R) in series. First, the equivalent circuit $I = \frac{V}{R} + \frac{dV}{dt} C$ fits well with the I-V curve (**Figure 3.2-C top**) despite a slightly larger slope at the curve's tail (<-0.3V) because of a marginal hydrogen generation reaction process (reaction barrier E^0= -0.828V vs. SHE) under slightly alkaline conditions with a pH of 7.4 in the 1× PBS[66]. This additional reaction tail can introduce a charge transfer resistance term at the electrolyte-electrode interface. From the I-V curve, the capacitance C is estimated at $C \cong 1.8 \times 10^{-3}$ F from the area capacitance using the following relation $C = C_a A$ with $C_a = \frac{\int I \, dV}{2A \cdot \gamma \cdot \Delta V}$, where I is current, V is voltage potential, A is the area of working electrode in EC cell, and γ is scan rate (V/s). The estimated C from the I-V curve encompasses the electrical double-layer capacitance of all the electrolyte-metal surfaces. Second, the elastic scattering peak at ≈0 cm^{-1} has a negligible voltage modulation. Third, PE-VRS signals at ≈270 cm^{-1} from Au-Cl surface bonds have a positive linear dependence on potential changes on the positive voltage side. Interestingly, PE-VRS signals become less sensitive to electrode potential changes on the negative

voltage side, suggesting the interfacial Au-Cl bond formation-deformation processes depend on the electrode potential polarities[67]. Fourth, the PE-ERS pseudo-peak signal at ≈87 cm^{-1} shows a negative linear dependence on potential changes with different voltage modulation slopes on the positive (≈30 % V^{-1}) and the negative (≈15 % V^{-1}) voltage sides, suggesting that interfacial charging-discharging processes also depend on the electrode potential polarities. The data shown in **Figure 3.2-C** originates from a single cycle measurement (from 60 s to 100 s). The coefficient of variations for positive and negative PE-ERS modulation slopes are 4.1% and 3.7%, respectively. Next, the broadband emission signal integrated from ≈600 cm^{-1} to ≈1200 cm^{-1} exhibits a negative linear voltage dependence with different voltage modulation rates on the positive (≈22 % V^{-1}) and negative (≈18 % V^{-1}) voltage sides, similar to the behaviors of the ERS pseudo-peak signal at ≈87 cm^{-1}. Last, the voltage-modulation slopes for both PE-VRS and PE-ERS signals change around ≈0 V, manifesting that the Au surface in 1× PBS with pH of ≈7.4 has a point of zero charge (PZC) potential U_{PZC} around ≈0 V in our measurements, which is reasonable as previous work shows with similar polycrystalline gold substrate[68]. This set of data and its modeling have been published in citation[41].

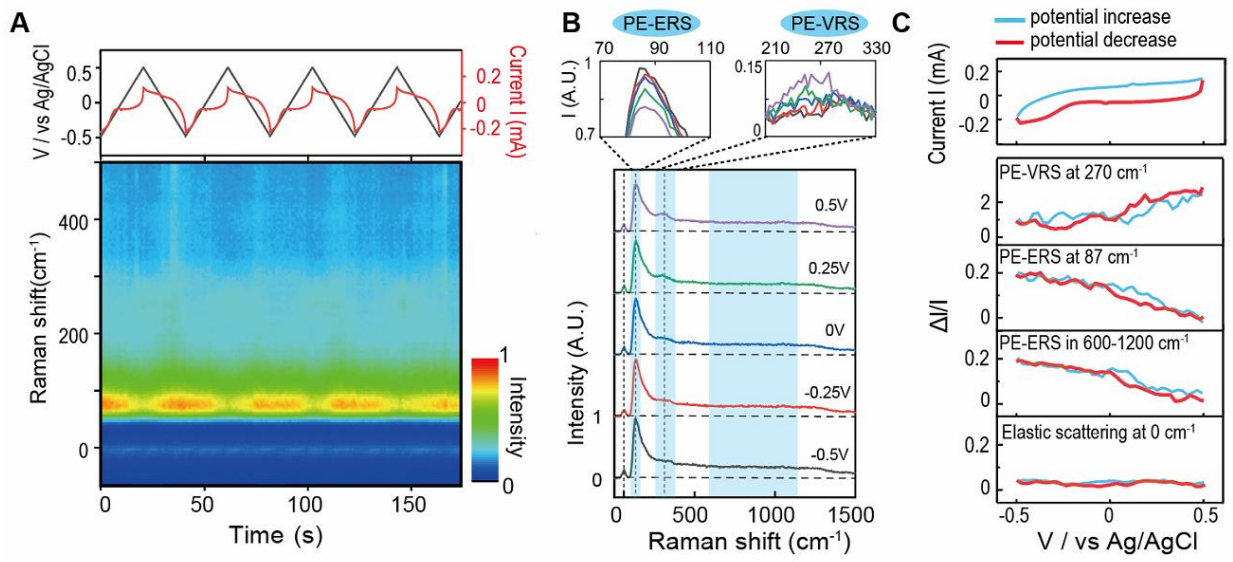

Figure 3.2 Electrode potential modulation of PE-ERS and PE-VRS signals from nano-optoelectrode Sample II in the electrolyte. (A) Time-dependent current measurements (top) under cyclic voltage (CV) sweeping between –0.5 and 0.5 V and time-dependent light emission spectra (bottom) under 785 nm laser excitation from the Sample II in the 1× PBS. (B) The measured light emission spectra (bottom) from the Sample II in the 1× PBS under 785 nm laser excitation at different applied potentials between -0.5 and 0.5 V and the corresponding zoomed-in view of PE-ERS pseudo peaks around ≈87 cm^{-1} (top left) and PE-VRS features around ≈270 cm^{-1} for Au-Cl bonds (top right) at different potentials. (C) The cyclic potential-dependent current (top) and normalized light emission intensities (bottom) for PE-VRS Au-Cl peak at ≈270 cm^{-1}, PE-ERS pseudo peak at ≈87 cm^{-1}, PE-ERS broad continuum integrated between 600 cm^{-1} and 1200 cm^{-1}, and elastic scattering peak at ≈0 cm^{-1}. Note: The coefficient of variations for positive and negative PE-ERS modulation slopes are 4.1% and 3.7%, respectively.

Chapter 4 Theoretical model & anaylsis

4.1 Faradaic modulation on PE-ERS & PE-ERS: EC-SERS on Sample I

The measurements of EC-SERS on Sample I reveal several notable observations. Firstly, well-defined Faradaic peaks, marked by an oxidation peak at ≈0.38 V and a reduction peak at ≈-0.22 V, become visible during voltage sweeps, indicative of the $AgCl(s) + e^- \rightleftharpoons Ag(s) + Cl^-(aq)$ redox reaction[54]. The ≈0.6 V redox peak-to-peak distance is considerably larger than that of ordinary Ag/AgCl cyclic voltammetry under similar conditions (≈0.152V)[57], implying that the redox reaction has a quasi-reversible behavior[11]. A probable explanation for the low electron transfer rate of the reaction is the formation of nanoporous electrolyte networks within Ag/AgCl matrices inside the Au-Ag-Au nanocavities during redox reactions, which limits the mass transport of ions involved in reactions and thereby impedes the reaction rate[56]. Secondly, we observe a PE-VRS peak at ≈258 cm^{-1}, linked to the stretching vibration of Ag-Cl bonds[55, 56]. The intensity of this peak during voltage modulation exhibits unsynchronized behavior in the Faradaic region for reduction or oxidation, with the PE-VRS peak intensity voltage preceding the Faradaic current peak voltage. We suggest that this PE-VRS peak relates to the (AgCl)* transition states (TS), having partial bonding with increased ability for its electron cloud distortion and enhanced polarizability changes compared to the steady-state Ag-Cl bond with a polar covalent nature, resulting in an increased VRS transition

dipole moment and amplified PE-VRS signals only during the redox reaction. This observation suggests that the opposing electrical field directions between reduction and oxidation cycles alter the microscopic VRS dipole moment orientation for (AgCl)* relative to the plasmonic electric field, resulting in varying PE-VRS emission intensities. In the non-Faradaic region, PE-VRS peak intensity increases linearly with voltage due to non-Faradaic capacitive modulation of metal surface charges at hotspots, consistent with our earlier study[58]. Thirdly, the PE-ERS pseudo peak at ≈87 cm^{-1} and tail intensities from

400 to 1400 cm^{-1} exhibit similar voltage-dependent behavior, indicating a common origin. Additionally, the PE-VRS peak at ≈258 cm^{-1} and the PE-ERS pseudo peak at ≈87 cm^{-1}

display identical voltage conditions for their peaks, dips, turn-on, and turn-off transitions, revealing a strong link between PE-VRS and PE-ERS events due to the generation of (AgCl)* TS in redox reactions. Notably, PE-ERS intensity changes are consistent in positive and negative voltage sweeps under Faradaic modulation, suggesting that varying electrical field directions during reduction and oxidation cycles do not impact the ERS dipole moment orientation for (AgCl)* relative to the plasmonic field. Finally, in contrast to redox-modulated PE-VRS and PE-ERS, the inelastic scattering peak at 0 cm^{-1} shows minor random fluctuations (≈10%), which is possibly due to plasmonic heating causing

local refractive index changes from local temperature fluctuation[59] or vapor/gas bubble formation[60], consequently altering the optical path and efficiency of elastic scattering signal collection.

To elucidate the dynamic PE-ERS and PE-VRS behaviors shown in **Figure 3.1**, we present a microscopic model in **Figure 4.1** that captures the evolution of these signals

during the electrochemical redox processes. Firstly, we depict microscopic transformations in the Faradaic redox reaction $AgCl(s) + e^- \rightleftharpoons Ag(s) + Cl^-(aq)$ at the electrode/electrolyte interface. In **Figure 4.1-A**, the potential energy is plotted against the generalized coordinate of Ag-Cl interatomic distance. As the coordinate approaches r_0, where energy is minimized, there is a strong coupling between the Ag sp band and Cl p orbitals, forming hybridized Ag-Cl orbitals with a 3.3 eV energy gap [69], and the steady-state Ag-Cl bond is polar covalent with a small Raman scattering cross-section. At r_{TS}, where energy peaks, the transition-state (AgCl)* complex forms with diminished coupling between the Ag sp band and Cl orbitals, producing negligible energy gaps between hybridized bonding and antibonding (AgCl)* orbitals, thus contributing extra PE-ERS signals. This hypothesis of (AgCl)* transition state electronic structure is supported by *ab initio* calculation work[10], in which one of the possible transition state configurations is described as a cluster on the interface with a continuous half-filled energy band. Additionally, the (AgCl)* TS's increased ability for electron cloud distortion results in enhanced polarizability changes and elevated VRS transition dipole moment $|\boldsymbol{\mu}^*|$, compared to the steady-state polar covalent Ag-Cl bond, thereby amplifying PE-VRS signals. This premise, where the (AgCl)* TS features filled bonding and unoccupied antibonding orbitals with negligible energy gaps and increased VRS transition dipole moment, undergirds our subsequent analysis of modulated PE-ERS and PE-VRS signals in the Faradaic process.

Figure 4.1-B presents a time-dependent, voltage-resolved view of measured current, PE-VRS, and PE-ERS intensities. A key takeaway from **Figure 4.1-B** is the discrepancy in peak and turn-on/turn-off voltages (or times) between the electrochemical current and the

PE-VRS/PE-ERS emission intensities. Combining this observation with insights from **Figure 3.1-C**, we infer that the behaviors of the PE-ERS and PE-VRS signals depend on the location of the emerging (AgCl)* TSs of the redox reaction within the plasmonic nanocavities. **Figure 4.1-C** depicts the FDTD estimated average PE-ERS and PE-VRS emission EFs, $|\boldsymbol{E_{SP}}|^4/|\boldsymbol{E_0}|^4$, as a function of location (x) across the Ag-AgCl nanoporous network within the top, middle, and bottom Au-Ag-Au nanogap cavities in NLPNAs. For simulations, we employ a first-order approximation using an ideal cylindrical NLNOE structure with a 50 nm radius and random dielectric nanoparticles within Ag layers to model the AgCl-Ag nanoporous network. The graph reveals a sharp decline in $|\boldsymbol{E_{SP}}|^4/|\boldsymbol{E_0}|^4$ values as x decreases.

In **Figure 4.1-D**, an illustrative diagram comprehensively explains PE-ERS and PE-VRS signal dynamics, highlighting the microscopic evolution between the steady-state of covalent Ag-Cl bonds or Ag and Cl elements and the TS of (AgCl)* complex within the nanoporous Ag/AgCl network at six distinct times (t_1 to t_6, as marked in **Figure 4.1-B**) during the oxidation and reduction processes. At t_1 and t_4, preceding the onset of oxidation and reduction, respectively, PE-ERS signals are modulated by voltage due to capacitive charging/discharging at the metal surface, whereas PE-VRS signals remain unaffected in the absence of TSs. At t_2 and t_5, the initiation of the $AgCl(s) + e^- \rightleftharpoons Ag(s) + Cl^-(aq)$ redox reaction occurs, marked by increased Faradaic current and peak intensities of PE-ERS and PE-VRS. At t_3 and t_6, though the Faradaic current reaches its peak, the intensities of PE-ERS and PE-VRS signals begin to decrease.

Let us elucidate how the (AgCl)* TS contributes to the emission intensity of the PE-ERS signal. The (AgCl)* TSs typically involve the hybridization between Ag sp bands near the Fermi level and the Cl atomic orbitals, leading to continuous energy states that offer a new trajectory for electron transition-relaxation, thereby enhancing PE-ERS intensity. To systematically analyze contributions from different electron transition pathways to the total PE-ERS intensity, $I_{ERS}(\delta\omega, r, \Delta)$, we introduce the following equation:

$$
\begin{aligned}
I_{ERS}(\delta\omega,r,\Delta) &= I_{ERS}^{m}(\delta\omega,r) + I_{ERS}^{TS}(\delta\omega,r,\Delta) + I_{ERS}^{m-TS}(\delta\omega,r,\Delta) \\
&= f_{SP}(\delta\omega,r)\Big\{Q_m\int_0^{\infty} g_m(E)f_T(E)g_m(E+\hbar\delta\omega)[1-f_T(E)]dE \\
&+ Q_{TS}\int_0^{\infty} g_{TS}^{\Delta}(E)f_T(E)g_{TS}^{\Delta}(E+\hbar\delta\omega)[1-f_T(E)]dE \\
&+ Q_{TS\to m}\int_0^{\infty} g_{TS}^{\Delta}(E)f_T(E)g_m(E+\hbar\delta\omega)[1-f_T(E)]dE \\
&+ Q_{m\to TS}\int_0^{\infty} g_m(E)f_T(E)g_{TS}^{\Delta}(E+\hbar\delta\omega)[1-f_T(E)]dE\Big\}
\end{aligned}
$$

This equation categorizes PE-ERS processes into three groups based on electron transition pathways. Here, $f_{SP}(\delta\omega, r) \approx |\boldsymbol{E_{SP}}(\delta\omega, r)|^4/|\boldsymbol{E_0}|^4$ represents the PE-ERS EFs at the shifted frequency $\delta\omega$ and position r. The term $g_m(E)$ denotes the electronic density of states for metal (Ag) sp-band at energy E, while $g_{TS}^{\Delta}(E)$ represents the electronic density of states for hybridized (AgCl)* TSs with an energy bandgap of Δ and centered at energy E. Specifically, I_{ERS}^{m} describes the PE-ERS process involving

transitions solely within the Ag sp band. In contrast, I_{ERS}^{TS} and I_{ERS}^{m-TS} involve ERS excitation-emission transitions mediated by (AgCl)* TSs, with the former accounting for both initial and final states to be TSs, and the latter accounting for one of the initial and final states to be TS. $f_T(E)$ represents the Fermi-Dirac distribution, while Q_m, Q_{TS}, $Q_{TS\to m}$ and $Q_{m\to TS}$ represent each process's corresponding ERS cross-section constant.

Notably, I_{ERS}^{m} depends on the non-Faradaic capacitive charging and discharging process but not the Faradaic redox process. In contrast, I_{ERS}^{TS} and I_{ERS}^{m-TS} can increase due to the formation of hybridized (AgCl)* TSs with continuous energy levels, providing an additional density of states through the atom's p orbitals. When a steady-state covalent Ag-Cl bond is formed, strong interatomic hybridization induces the bonding and antibonding states with a large energy gap, ceasing the contribution to PE-ERS signals. Therefore, the additional PE-ERS terms, I_{ERS}^{TS} and I_{ERS}^{m-TS}, only appear when (AgCl)* TSs are formed during the Faradaic redox process. These features are depicted in the top row of **Figure 4.1-D**, where the transition pathways to PE-ERS signals, including I_{ERS}^{m} , I_{ERS}^{TS} and I_{ERS}^{m-TS}, are color-coded.

Next, we focus on the behavior of PE-VRS during the Faradaic redox process. Similar to PE-ERS, PE-VRS emerges only in the presence of the (AgCl)* TSs because weakly coupled electrons in (AgCl)* TSs have an augmented capacity for electron cloud

distortion to enhance polarizability changes and thus VRS transition dipole moment $|\boldsymbol{\mu}^*|$, compared to the polar covalent Ag-Cl bond in the steady-state. Therefore, PE-VRS follows PE-ERS trends with emerged (AgCl)* TSs during the redox reaction. However, a distinct feature in PE-VRS is the differing amplitude of Faradaic modulation in various reaction directions, which may arise from the (AgCl)* TSs' varying average orientations due to the attractive or repulsive electrostatic forces of positive or negative metal electrode voltages, respectively. As shown in the bottom plots of **Figure 4.1-D**, the (AgCl)* TSs appear at the boundary of Ag-AgCl porous network channels with different orientations due to the polarity change of induced charges at the metal surface, leading to different alignments of the VRS dipole moment $\boldsymbol{\mu}^*$ with the plasmon-driven electric field $\boldsymbol{E_{SP}}$ in hotspots. As a result, the Faradaic modulation amplitude is more pronounced in the reduction direction compared to the oxidation direction.

Next, we examine how near-field enhancements influence PE-ERS and PE-VRS signals. Plasmonic enhancements for PE-ERS and PE-VRS signals are proportional to $|\boldsymbol{E_{SP}}|^4/|\boldsymbol{E_0}|^4$. As shown in **Figure 4.1-C**, $|\boldsymbol{E_{SP}}|^4/|\boldsymbol{E_0}|^4$ decays exponentially along the nanoporous Ag/AgCl network inward of the Au-Ag-Ag nanocavities. As oxidation/reduction processes proceed, the positions of redox generated (AgCl)* TSs move inward, as depicted in the middle row of **Figure 4.1-D**. As the reaction progresses, this inward movement results in weaker field enhancements on PE-ERS and PE-VRS. Coupled with the emergence of TS in the Faradaic process, the peak intensities of PE-ERS and PE-VRS signals diverge from the current, as evident in **Figure 4.1-B**.

Lastly, we briefly revisit the non-Faradaic modulation of PE-ERS and PE-VRS, which we discussed extensively previously [58]. In **Figure 4.1-B**, dashed lines beneath the curves indicate the effects of the non-Faradaic process. In the non-Faradaic process, the PE-ERS intensity from metal hotspots, $I_{ERS}^{m}(\delta\omega, r)$, declines linearly with voltage due to the capacitive voltage modulation of the induced charge density on the electrode surface[41]. This surface charge modulation causes a shift in the Fermi energy level on the Ag surface, shown in the top row of **Figure 4.1-D**. Since the voltage-modulated surface charge within the Debye length overlaps with the decay length of the plasmonic field, PE-ERS signals show a high sensitivity to both Faradaic and non-Faradaic voltage modulation processes.

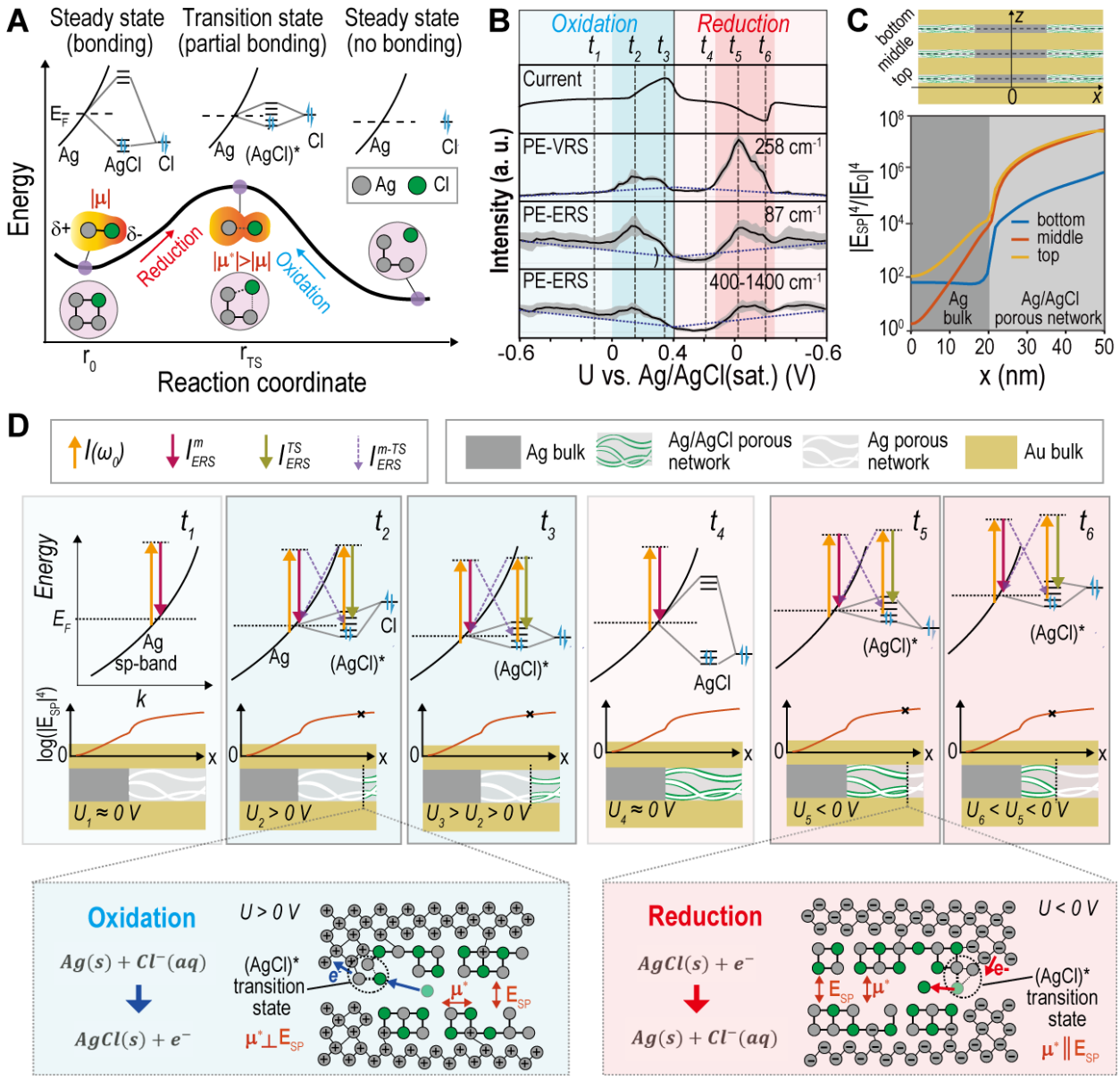

Figure 4.1. Illustration of the correlated PE-ERS and PE-VRS monitoring of transition states during electrochemical redox reactions within plasmonic nanocavities. (A) Diagram depicting the interfacial electronic and vibrational structures linked to Ag-Cl bond dynamics during the electrochemical redox reaction, within Au/Ag/Au nanogap hotspots at the electrode-electrolyte interface. (B) Time-dependent voltage-resolved representation of measured electrical current, PE-VRS, and PE-ERS intensities. Plots show average signals, and shaded regions indicate standard deviation over five cycles at different voltages (standard deviation for current not shown due to <1% variation). Blue and red shading indicates oxidation (potential increase) and reduction (potential decrease) processes, respectively. The labels of t_1 to t_6 represent six characteristic times within one

cycle of redox reaction. The dashed line beneath the PE-ERS and PE-VRS signal curves represents the non-Faradaic voltage modulation-induced contributions. (C) The FDTD-

estimated near-field enhancement factor $|\boldsymbol{E_{SP}}|^4/|\boldsymbol{E_0}|^4$ as a function of x position for PE-ERS and PE-VRS emissions within the Au-Ag-Au nanogap with Ag/AgCl nanoporous networks. (D) Illustration of microscopic changes between the steady-state covalent Ag-Cl bonds (or Ag and Cl elements) and the (AgCl)* transition state (TS) within the nanoporous Ag/AgCl network at six representative times (t_1 to t_6) corresponding to Fig. 4B.

4.2 Non-Faradaic modulation on PE-ERS & PE-ERS: EC-SERS on Sample II

To understand the voltage modulation behaviors for PE-ERS and PE-VRS signals within the non-Faradaic process from the nano-optoelectrode (Sample II), we need to consider optical, electronic, and ionic activities in the plasmonic hotspots at the metal-electrolyte interface. As illustrated in **Figure 4.2-A**, the laser excitation of plasmonic modes in Sample II can concentrate intense optical fields in multi-nanogap MIM nanocavities[40] to generate PE-VRS signals from Au-Cl surface bonds and PE-ERS signals from Au sp-band electron-hole pairs. Like PE-VRS, surface plasmon modes can simultaneously enhance excitation (ω_0) and emission (ω) transitions for PE-ERS to realize a significant enhancement factor $F(\omega_0,\omega,\boldsymbol{r}) \approx |E_{SP}(\omega_0,\boldsymbol{r})|^2 \cdot |E_{SP}(\omega,\boldsymbol{r})|^2 \approx |E_{SP}(\omega_0,\boldsymbol{r})|^4$, where $|E_{SP}|$ is the local electric field amplitude at position $\boldsymbol{r}$ inside the metal. In this way, we can express the PE-ERS flux density as,

$$i_{PE-ERS}(\omega_0,\omega,\boldsymbol{r}) \approx F(\boldsymbol{r}) \cdot i_{in}(\omega_0) \cdot \sigma_{ERS}(\omega_0,\omega) \cdot \left| e^{-\frac{\hbar(\omega_0-\omega)}{k_B T}} - 1 \right|^{-1} \cdot n(\boldsymbol{r}) = F(\boldsymbol{r}) \cdot K \cdot n(\boldsymbol{r}), \quad (1)$$

where i_{in} is the incident laser flux density, σ_{ERS} is the cross section coefficient for an ERS event, $\left|e^{-\frac{\hbar(\omega_0-\omega)}{k_BT}}-1\right|^{-1}$ is the Bose-Einstein distribution of the electron-hole pairs at Stokes-shifted frequency $\Delta\omega = \omega_0 - \omega$, and $n(\boldsymbol{r})$ is the local free electron density in the metal. By defining $K = i_{in}(\omega_0)\cdot\sigma_{ERS}(\omega_0,\omega)\cdot\left|e^{-\frac{\hbar(\omega_0-\omega)}{k_BT}}-1\right|^{-1}$, the PE-ERS flux density becomes a position-dependent function as $i_{PE-ERS} = F(\boldsymbol{r})\cdot K\cdot n(\boldsymbol{r})$[62]. Since $n(\boldsymbol{r})$ directly couples with the local Fermi energy level as $E_F(\boldsymbol{r}) = \frac{\hbar^2}{2m}[3\pi^2 n(\boldsymbol{r})]^{2/3}$, the change of electrode potential *U* at the electrolyte interface can modulate $E_F(\boldsymbol{r})$ and accordingly $n(\boldsymbol{r})$ within the Debye length d_D^m (≈0.15 nm for Au) at the metal surface[70, 71]. Thus, as illustrated in **Figure 4.2-A&B**, the electrode potential modulation ($U_1 < U_2$) can change PE-ERS intensity from the hotspots in which the metal is electrically connected to the working electrode substrate and exposed to the electrolyte.

Figure 4.2-C illustrates that the change between positive and negative electrode potentials will reverse the electrical polarities of induced metal surface charges and ionic species in the electrical double layer (EDL) at the electrode-electrolyte interface. As a general model, the EDL structure consists of (i) the Stern layer with the inner Helmholtz plane (IHP) for specifically adsorbed ions and the outer Helmholtz plane (OHP) for non-specifically adsorbed ions and (ii) the diffuse layer for free-moving ions. Under $U > 0$ V, the positively charged metal surface can electrostatically attract negatively charged ions to increase the surface density of both specifically and non-specifically adsorbed Cl^- ions in the Stern layer [64, 72]. The increased surface density of specifically adsorbed Cl^- ions under positive potential can lead to more non-covalent Au-Cl surface bonds at the Au surface. On the other hand, applying negative electrode potentials (e.g., $U < -0.5$ V) will

increase the number of specifically and non-specifically adsorbed positive ions (e.g., Na^+) and deplete the non-covalent Au-Cl surface bonds, while those more stable covalent Au-Cl surface bonds can remain. Such a scheme can explain the observation in **Figure 3.2-C** that PE-VRS signals at ≈270 cm^{-1} show a positive modulation rate on positive voltages by forming non-covalent Au-Cl surface bonds but an insensitive modulation on negative voltages due to the depletion of non-covalent Au-Cl surface bonds. Furthermore, since Cl^- and Na^+ ions have different electric susceptibility values, the polarity change of electrode potential can modulate the local dielectric permittivity ϵ_D^l in EDL environment

by switching the types of ionic species which occupy the Stern layer, which will further affect the voltage modulation rates for PE-ERS signals, as discussed later.

As illustrated in **Figure 4.1-D-top**, applying a positive electrode potential (U > 0 V) can drastically distort the electrical free energy *Φ(z)* across the interfacial region of the metal Debye length d_D^m (≈ 0.15 nm for Au) and the electrolyte Debye length d_D^l (≈ 0.79 nm for

1× PBS, ionic strength: ≈0.15 mol/L). Accordingly, local Fermi energy $E_F(z)$ and local free electron density *n(z)* can be electrically modulated within d_D^m at the metal surface. It

should be noted here that $E_F(z)$ may also be modulated due to the adsorbed halide ions [73]. In contrast, **Figure 4.1-D-bottom** shows that the local electric field amplitude $|E_{SP}|$ for

the surface plasmon mode exponentially decreases from the metal-liquid interface with the characteristic penetration lengths d_{SP}^m and d_{SP}^l on the metal and electrolyte sides. In

this experiment, d_{SP}^m can be approximated as ≈5 nm according to the mode confinement

dimension for the surface plasmons supported in the MIM nanocavity[74]. As a first-order approximation, we can express the *z*-dependent PE-ERS enhancement factor as

$$F(z) \approx |E_{SP}(z)|^4 \approx |E_{SP}(z=0)|^4 \cdot e^{-\frac{4z}{d_{SP}^m}} = F_{max} \cdot e^{-\frac{4z}{d_{SP}^m}} \quad (2).$$

Using **Eq. 1** and **Eq. 2,** we can express the total PE-ERS flux from a plasmonic nanocavity hotspot with a mode surface area A_{tot} as:

$$I_{PE-ERS} \approx \int_0^\infty i_{PE-ERS}(z) \cdot A_{tot} \cdot dz \approx K \cdot F_{max} \cdot A_{tot} \cdot \int_0^\infty n(z) \cdot e^{-\frac{4z}{d_{SP}^m}} \cdot dz \quad (3).$$

In the condition with a zero electrode surface potential ($U_0 \approx U_{PZC} \approx 0$ V), the free electron density $n(z) = n(U_0)$ is uniform inside the metal, and we can use **Eqs. 2-3** to express the PE-ERS flux as

$$I_{PE-ERS}(U_0) \approx K \cdot F_{max} \cdot A_{tot} \cdot n(U_0) \cdot \int_0^\infty e^{-\frac{4z}{d_{SP}^m}} \cdot dz = \frac{1}{4} \cdot K \cdot F_{max} \cdot A_{tot} \cdot n(U_0) \cdot d_{SP}^m$$

(4).

On the other side, with a nonzero electrode potential ($U \neq 0$ V), we can decompose the plasmonic hotspot mode surface into (i) the region exposed to the electrolyte with an area of A_{exp}, and (ii) the embedded region with an area of $A_{tot} - A_{exp}$. Within the electrolyte-exposed hotspot region under electrode potential U, we can approximate the z-dependent free electron density profile $n(z)$ as (i) $n(U)$ within the metal Debye length $|z| < d_D^m$, and (ii) $n(U_0)$ outside the metal Debye length $|z| > d_D^m$. By defining a local EDL capacitance at the plasmonic hotspot as

$$C^* \approx \frac{\epsilon_D^l}{d_D^l} \cdot A_{exp} \quad (5),$$

we can express the free electron density change with electrode potential modulation within the metal Debye length as

$$\Delta n = n(U) - n(U_0) \approx \frac{C^* \cdot (U - U_0)}{-e \cdot A_{exp} \cdot d_D^m} \approx \frac{(U - U_0)}{-e \cdot d_D^m} \cdot \frac{\epsilon_D^l}{d_D^l} \quad (6).$$

Using **Eqs. 4**-**6**, we can model the potential modulated PE-ERS flux from a hotspot as

$$\Delta I_{PE-ERS} = I_{PE-ERS}(U) - I_{PE-ERS}(U_0) \approx K \cdot F_{max} \cdot A_{exp} \cdot \int_0^{d_D^m} [n(U) - n(U_0)] \cdot e^{-\frac{4z}{d_{SP}^m}} \cdot dz$$

$$\approx K \cdot F_{max} \cdot A_{exp} \cdot [n(U) - n(U_0)] \cdot d_D^m \approx K \cdot F_{max} \cdot \frac{C^* \cdot (U - U_0)}{-e} \approx K \cdot F_{max} \cdot \frac{(U - U_0) \cdot A_{exp}}{-e} \cdot \frac{\epsilon_D^l}{d_D^l}$$

(7).

Using **Eqs. 4** & **7**, the modulation ratio for PE-ERS flux from a hotspot can be expressed as

$$\frac{\Delta I_{PE-ERS}}{I_{PE-ERS}(U_0)} \approx -\frac{4 \cdot (U - U_0)}{n(U_0) \cdot e} \cdot \frac{1}{d_{SP}^m} \cdot \frac{C^*}{A_{tot}} \approx -\frac{4 \cdot (U - U_0)}{n(U_0) \cdot e} \cdot \frac{\epsilon_D^l}{d_D^l} \cdot \frac{1}{d_{SP}^m} \cdot \frac{A_{exp}}{A_{tot}} \quad (8).$$

Our analytical model in **Eq. 8** can reasonably agree with the observations in **Figure 3C**. First, the PE-ERS signal modulation ratio $\frac{\Delta I_{PE-ERS}(\Delta U)}{I_{PE-ERS}(U_0)}$ has a negative linear dependence on the electrode potential U, considering $U_0 \approx U_{PZC} \approx 0$ V in our measurements. Second, the potential modulation slope $\frac{\Delta I_{PE-ERS}(\Delta U)}{I_{PE-ERS}(U_0)}$ depends on the local dielectric permittivity ϵ_D^l in the EDL and thus can change values by switching polarities of electrode surface potential and ionic species with different susceptibilities in the Stern layer[11].

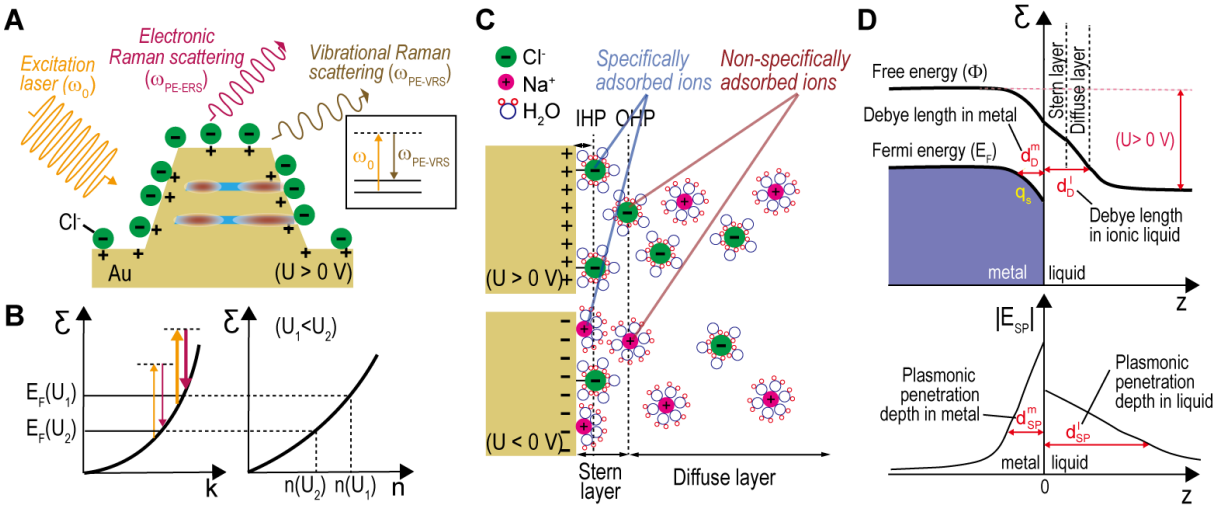

Figure 4.2. The mechanism for electrode potential modulation of PE-ERS signals from plasmonic hotspots at the metal-electrolyte interface. (A) The scheme of PE-ERS and PE-VRS light emission from plasmonic hotspots in the nano-optoelectrode (Sample II) with an applied electrode potential U > 0 V in the electrolyte. The inset shows the energy diagram of the VRS process. (B) The energy diagram scheme illustrates that the electrode penitential difference ($U_1 < U_2$) can change the ERS intensity by shifting the Fermi energy E_F and free electron density n at the metal surface. (C) The scheme of the local electrochemical environment at the electrode-electrolyte interface with positive (top) and negative (bottom) electrode surface potential U and induced surface charge. (D) The scheme of position-dependent energy distribution with a positive electrode potential ($U >$ 0 V) (top) and surface plasmon electric field intensity $|E|^2$ profile (bottom) at the electrode-electrolyte interface.

Significantly, **Eq. 8** predicts that the PE-ERS voltage modulation rate $\frac{\Delta I_{PE-ERS}(\Delta U)}{\Delta U \cdot I_{PE-ERS}(U_0)}$ is

proportional to the local capacitance $C^* \approx \frac{\epsilon_D^l}{d_D^l} \cdot A_{exp}$ at the electrolyte-exposed plasmonic

hotspot region and thus depends on the local electrolyte capacitive characteristics in $\frac{\epsilon_D^l}{d_D^l}$.

Since increasing ion concentration P in the electrolyte can decrease d_D^l and increase ϵ_D^l,

we expect that $\frac{\Delta I_{PE-ERS}(\Delta U)}{\Delta U \cdot I_{PE-ERS}(U_0)}$ can increase with ion concentration *P* due to increased C^*.

To validate this model prediction, we conducted experiments to measure the electrode potential *U*-dependent $\frac{\Delta I_{PE-ERS}(\Delta U)}{I_{PE-ERS}(U_0)}$ in electrolytes with different ion concentrations *P*, including 1× PBS (P0 = 150 mol/m^3), diluted 0.1× PBS (P1 = 15 mol/m^3), diluted 0.01× PBS (P2 = 1.5 mol/m^3), and diluted 0.001× PBS (P3 = 0.15 mol/m^3) solutions. **Figure 4.3-A** shows the experimental *U* vs. $\frac{\Delta I_{PE-ERS}(\Delta U)}{I_{PE-ERS}(U_0)}$ results from *in situ* EC-SERS measurements of NLNOEs in electrolytes of different *P* under cyclic voltage sweeping between –0.5 V and 0.5 V at a ≈50 mV/s scan rate for five cycles. There are several observations. First, $\frac{\Delta I_{PE-ERS}(\Delta U)}{I_{PE-ERS}(U_0)}$ has a negative linear dependence on *U* but with a reduced slope amplitude at lower ion concentrations *P*. Second, in higher ion concentration electrolytes (150 mol/m^3 and 15 mol/m^3), the PE-ERS voltage modulation slope amplitude is higher in positive than negative electrode potentials, while the slope difference significantly drops in lower ion concentration electrolytes (1.5 mol/m^3 and 0.15 mol/m^3).

By defining a slope coefficient as $b_p^{*,\pm} = \frac{4}{n(U_0)\cdot e} \cdot \frac{1}{d_{SP}^m} \cdot \frac{C_p^{*,\pm}}{A_{tot}}$ at positive (+) and negative (-) electrode potentials, we can express **Eq. (8)** as

$$\frac{\Delta I_P(U)}{I_P(U_0)} \approx -b_p^{*,\pm} \cdot (U - U_0) \qquad (9),$$

to fit measurements as red lines in **Figure 4.3-A** and extract the fitted $b_p^{*,\pm}$ slope coefficients at different ion concentrations *P* and electrode polarities ($\pm$). Based on $b_p^{*,\pm}/b_{p0}^{*,+} = C_p^{*,\pm}/C_{p0}^{*,+}$ in a ratiometric normalization with the P_0 values from 1×PBS, **Figure 4.3-B** quantitively illustrates the effects of ion concentrations *P* and electrode potential polarities ($\pm$) on the PE-ERS retrieved local capacitance values $C_p^{*,\pm}/C_{p0}^{*,+}$ from nanoscale plasmonic hotspots, which reveals several crucial points by comparing with the cyclic I-V extracted macroscopic capacitance C_P/C_{P0} from Sample II with cm^2-scale area. First, both macroscopic capacitance C_P/C_{P0} and microscopic capacitance $C_p^{*,\pm}/C_{p0}^{*,+}$ values decrease with decreasing *P*, manifesting that $\frac{\epsilon_D^l}{d_D^l}$ of the electrolyte EDL depends on ion concentration *P*. Second, the observation of much-increased differences between $C_p^{*,+}/C_{p0}^{*,+}$ and $C_p^{*,-}/C_{p0}^{*,+}$ only at higher ion concentrations suggest that a short electrolyte Debye length d_D^l (e.g., ≈ 0.79 nm for 150 mol/m^3, ≈ 2.5 nm for for 15 mol/m^3) may cause a more significant effect of the difference in electric susceptibility and, accordingly, dielectric permittivity between specifically/non-specifically adsorbed Cl^- and Na^+ species within the Stern layer under opposite *U* polarities on local capacitance values at hotspots[75, 76]. Overall, the agreement between the experimental data and the fitting results with different ion concentrations substantiates the credibility of the developed model.

As shown in **Figure 4.3-C**, we measured the temporal responses of the PE-ERS pseudo peak at ≈87 cm^{-1} and Au-Cl PE-VRS peak at ≈270 cm^{-1} under voltage square waves alternating at ± 0.3 V, 0 V, or $\pm$ 0.5 V in 1× PBS with an integration time of 0.5 s. Similar to measurements under cyclic sweeping conditions in **Figure 3.2-C**, the square-wave inputs produce more significant voltage modulation of the PE-ERS and PE-VRS signals

under the positive ($U > 0$ V) than negative electrode potentials ($U < 0$ V) with similar voltage modulation rates, manifesting that the underlying electrode potential modulation mechanisms for PE-ERS and PE-VRS signals remain the same under different input voltage shapes.

Chapter 5 Summarization & Outlook

For the Faradaic process, our study represents a significant advancement for *in situ* EC-SERS technology via our nano-optoelectrode, enabling the probing of transition state information during redox reactions within plasmonic nanocavities through the integration of PE-ERS and PE-VRS signals. This dual-signal approach provides a nuanced understanding of electronic states at electrode/electrolyte interfaces, expanding EC-SERS applications. Our innovative two-tier nano-optoelectrode design aligns reaction sites within plasmonic nanogap modes' hotspots, facilitating efficient reaction monitoring through spectral measurements. The nano-optoelectrode design's adaptability allows for substituting the silver layer with other reactant materials, supporting the study of a broader range of reactions. While further research in controlling electrochemical interfacial properties and optimizing the nano-optoelectrode design for enhanced signal sensitivity is needed, our study is a keystone in elevating the EC-SERS methods for real-time monitoring of various electrochemical and electrocatalytic processes at electrode interfaces.

For the non-Faradaic electrochemical modulation on our nano-optoelectrode, we note that the PE-ERS signals possess much higher voltage modulation sensitivity than the traditional elastic scattering-based plasmonic devices[77] because the tightly confined voltage-induced surface electron density changes within the metal Debye length d_D^m

(≈0.15 nm) have a high spatial overlap with the plasmonic enhancement profile $|E_{SP}|^4 \cdot e^{-\frac{4z}{d_{SP}^m}}$ for PE-ERS signals with a tight $|E_{SP}|^4$-related optical depth in the metal

of $\frac{d_{SP}^{m}}{4}$. Meanwhile, for the elastic channel, the resonance wavelength shifts or intensity changes are determined by the total bulk charge density changes of the plasmonic resonator[77], causing weaker voltage modulation rates. In conclusion, we have demonstrated a substantial capacitive voltage modulation (up to ≈30 % V^{-1}) of nanoplasmonic metal luminescence associated with PE-ERS signals from hotspots at the electrode-electrolyte interface using our nano-optoelectrode. We have developed a simple phenomenological model to capture critical plasmonic, electronic, and ionic characteristics at the metal-electrolyte interface to understand experimental observations, which can also provide guidelines for further performance improvement. Significantly, this study reveals that the voltage modulation of PE-ERS metal luminescence signals originates from the spatial overlap between the plasmonic mode $|E_{SP}|^4$ penetration depth $\frac{d_{SP}^{m}}{4}$ and electronic Debye length d_D^m for the electrolyte-exposed metal surface at hotspots and can follow the changes in microscopic capacitive characteristics (e.g., local electrolyte Debye length d_D^l, local dielectric permittivity ϵ_D^l) at the electrode-electrolyte interface. Although this work focuses on modeling and analyzing PE-ERS from Au-based MIM nanocavity hotspots under NIR laser excitation, the developed model can be generalized to accommodate other possible plasmon-enhanced metal luminescence processes, such as intraband and interband photoluminescence of hot carriers in the metal. This generalization is possible because these plasmon-enhanced metal luminescence mechanisms involve plasmonic near-field enhancements and the transition of electrons near the Fermi level. While additional work will be needed, for example, to improve

signal brightness and voltage sensitivity by optimizing nano-optoelectrode designs, the current work represents a critical step toward the general application of nanoplasmonic metal luminescence in optical voltage biosensing, hybrid optical-electrical signal transduction, and interfacial monitoring of electrochemical processes

1. Dantus, M.; Rosker, M. J.; Zewail, A. H., Real‐time femtosecond probing of ‘‘transition states’’ in chemical reactions. *The Journal of Chemical Physics* **1987,** *87* (4), 2395-2397.
2. Laidler, K. J., Just what is a transition state? *Journal of chemical Education* **1988,** *65* (6), 540.
3. Abidi, N.; Steinmann, S. N., How are transition states modeled in heterogeneous electrocatalysis? *Curr Opin Electroche* **2022,** *33*.
4. Chen, H. L.; Jia, C. C.; Zhu, X.; Yang, C.; Guo, X. F.; Stoddart, J. F., Reactions in single-molecule junctions. *Nat Rev Mater* **2023,** *8* (3), 165-185.
5. Bruno, G.; Melle, G.; Barbaglia, A.; Iachetta, G.; Melikov, R.; Perrone, M.; Dipalo, M.; De Angelis, F., All‐Optical and Label‐Free Stimulation of Action Potentials in Neurons and Cardiomyocytes by Plasmonic Porous Metamaterials. *Advanced Science* **2021,** *8* (21), 2100627.
6. Koo, K.-M.; Kim, C.-D.; Ju, F. N.; Kim, H.; Kim, C.-H.; Kim, T.-H., Recent Advances in Electrochemical Biosensors for Monitoring Animal Cell Function and Viability. *Biosensors* **2022,** *12* (12), 1162.
7. Zhang, X.; Cheng, X.; Zhang, Q., Nanostructured energy materials for electrochemical energy conversion and storage: a review. *Journal of energy chemistry* **2016,** *25* (6), 967-984.
8. Cheng, P.; Zhong, D.; Zewail, A. H., Femtosecond real‐time probing of reactions. XXI. Direct observation of transition‐state dynamics and structure in charge‐transfer reactions. *The Journal of chemical physics* **1996,** *105* (15), 6216-6248.
9. Cocker, T. L.; Peller, D.; Yu, P.; Repp, J.; Huber, R., Tracking the ultrafast motion of a single molecule by femtosecond orbital imaging. *Nature* **2016,** *539* (7628), 263-+.
10. Ma, X.; Dai, Y.; Guo, M.; Zhu, Y.; Huang, B., Insights into the adsorption and energy transfer of Ag clusters on the AgCl (100) surface. *Physical Chemistry Chemical Physics* **2013,** *15* (22), 8722-8731.
11. Bard, A. J.; Faulkner, L. R.; White, H. S., *Electrochemical methods: fundamentals and applications*. John Wiley & Sons: 2022.
12. Kaim, W.; Fiedler, J., Spectroelectrochemistry: the best of two worlds. *Chemical Society Reviews* **2009,** *38* (12), 3373-3382.
13. Lozeman, J. J. A.; Fuhrer, P.; Olthuis, W.; Odijk, M., Spectroelectrochemistry, the future of visualizing electrode processes by hyphenating electrochemistry with spectroscopic techniques. *Analyst* **2020,** *145* (7), 2482-2509.
14. Zhai, Y. L.; Zhu, Z. J.; Zhou, S. S.; Zhu, C. Z.; Dong, S. J., Recent advances in spectroelectrochemistry. *Nanoscale* **2018,** *10* (7), 3089-3111.
15. Yue, K.; Weipeng, W.; Tian, M.; Ting, Z.; Junxian, C.; Zhengjun, Z., Recent advances in Raman and surface enhanced Raman spectroelectrochemistry. *Front Nanotechnol* **2023,** *4*.
16. Pitarke, J. M.; Silkin, V. M.; Chulkov, E. V.; Echenique, P. M., Theory of surface plasmons and surface-plasmon polaritons. *Rep Prog Phys* **2007,** *70* (1), 1-87.
17. Kinkhabwala, A.; Yu, Z. F.; Fan, S. H.; Avlasevich, Y.; Mullen, K.; Moerner, W. E., Large single-molecule fluorescence enhancements produced by a bowtie nanoantenna. *Nature Photonics* **2009,** *3* (11), 654-657.
18. Kauranen, M.; Zayats, A. V., Nonlinear plasmonics. *Nature Photonics* **2012,** *6* (11), 737-748.
19. Sun, G.; Khurgin, J. B., Origin of giant difference between fluorescence, resonance, and nonresonance Raman scattering enhancement by surface plasmons. *Phys Rev A* **2012,** *85* (6).

20. Aouani, H.; Rahmani, M.; Navarro-Cia, M.; Maier, S. A., Third-harmonic-upconversion enhancement from a single semiconductor nanoparticle coupled to a plasmonic antenna. *Nature Nanotechnology* **2014,** *9* (4), 290-294.
21. Celebrano, M.; Wu, X. F.; Baselli, M.; Grossmann, S.; Biagioni, P.; Locatelli, A.; De Angelis, C.; Cerullo, G.; Osellame, R.; Hecht, B.; Duo, L.; Ciccacci, F.; Finazzi, M., Mode matching in multiresonant plasmonic nanoantennas for enhanced second harmonic generation. *Nature Nanotechnology* **2015,** *10* (5), 412-417.
22. Pelton, M., Modified spontaneous emission in nanophotonic structures. *Nat Photonics* **2015,** *9* (7), 427-435.
23. Tali, S. A. S.; Mudiyanselage, R. R. H. H.; Qian, Y. Z.; Smith, N. W. G.; Zhao, Y. M.; Morral, A.; Song, J. Y.; Nie, M. T.; Magill, B. A.; Khodaparast, G. A.; Zhou, W., Dual-Modal Nanoplasmonic Light Upconversion through Anti-Stokes Photoluminescence and Second-Harmonic Generation from Broadband Multiresonant Metal Nanocavities. *Acs Nano* **2023**.
24. Zhou, W.; Dridi, M.; Suh, J. Y.; Kim, C. H.; Co, D. T.; Wasielewski, M. R.; Schatz, G. C.; Odom, T. W., Lasing action in strongly coupled plasmonic nanocavity arrays. *Nature Nanotechnology* **2013,** *8* (7), 506-511.
25. Hugall, J. T.; Baumberg, J. J., Demonstrating Photoluminescence from Au is Electronic Inelastic Light Scattering of a Plasmonic Metal: The Origin of SERS Backgrounds. *Nano Letters* **2015,** *15* (4), 2600-2604.
26. Mahajan, S.; Cole, R. M.; Speed, J. D.; Pelfrey, S. H.; Russell, A. E.; Bartlett, P. N.; Barnett, S. M.; Baumberg, J. J., Understanding the Surface-Enhanced Raman Spectroscopy "Background". *J Phys Chem C* **2010,** *114* (16), 7242-7250.
27. Zong, C.; Xu, M.; Xu, L. J.; Wei, T.; Ma, X.; Zheng, X. S.; Hu, R.; Ren, B., Surface-Enhanced Raman Spectroscopy for Bioanalysis: Reliability and Challenges. *Chem Rev* **2018,** *118* (10), 4946-4980.
28. Di Martino, G.; Turek, V. A.; Lombardi, A.; Szabo, I.; de Nijs, B.; Kuhn, A.; Rosta, E.; Baumberg, J. J., Tracking Nanoelectrochemistry Using Individual Plasmonic Nanocavities. *Nano Letters* **2017,** *17* (8), 4840-4845.
29. Wilson, A. J.; Molina, N. Y.; Willets, K. A., Modification of the Electrochemical Properties of Nile Blue through Covalent Attachment to Gold As Revealed by Electrochemistry and SERS. *J Phys Chem C* **2016,** *120* (37), 21091-21098.
30. Shegai, T.; Vaskevich, A.; Rubinstein, I.; Haran, G., Raman Spectroelectrochemistry of Molecules within Individual Electromagnetic Hot Spots. *Journal of the American Chemical Society* **2009,** *131* (40), 14390-14398.
31. Do, H.; Kwon, S. R.; Fu, K. Y.; Morales-Soto, N.; Shrout, J. D.; Bohn, P. W., Electrochemical Surface-Enhanced Raman Spectroscopy of Pyocyanin Secreted by Pseudomonas aeruginosa Communities. *Langmuir* **2019,** *35* (21), 7043-7049.
32. Bindesri, S. D.; Alhatab, D. S.; Brosseau, C. L., Development of an electrochemical surface-enhanced Raman spectroscopy (EC-SERS) fabric-based plasmonic sensor for point-of-care diagnostics. *Analyst* **2018,** *143* (17), 4128-4135.
33. Yuan, T.; Ngoc, L. L. T.; van Nieuwkasteele, J.; Odijk, M.; van den Berg, A.; Permentier, H.; Bischoff, R.; Carlen, E. T., In Situ Surface-Enhanced Raman Spectroelectrochemical Analysis System with a Hemin Modified Nanostructured Gold Surface. *Analytical Chemistry* **2015,** *87* (5), 2588-2592.

34. Isogai, T.; Motobayashi, K.; Ikeda, K., A single spectroscopic probe for in situ analysis of electronic and vibrational information at both sides of electrode/electrolyte interfaces using surface-enhanced Raman scattering. *The Journal of Chemical Physics* **2021,** *155* (20), 204702.
35. Hill, C. M.; Bennett, R.; Zhou, C.; Street, S.; Zheng, J.; Pan, S., Single Ag nanoparticle spectroelectrochemistry via dark-field scattering and fluorescence microscopies. *The Journal of Physical Chemistry C* **2015,** *119* (12), 6760-6768.
36. Searles, E. K.; Gomez, E.; Lee, S.; Ostovar, B.; Link, S.; Landes, C. F., Single-Particle Photoluminescence and Dark-Field Scattering during Charge Density Tuning. *The Journal of Physical Chemistry Letters 14*, 318-325.
37. Isogai, T.; Motobayashi, K.; Ikeda, K., A single spectroscopic probe for in situ analysis of electronic and vibrational information at both sides of electrode/electrolyte interfaces using surface-enhanced Raman scattering. *J Chem Phys* **2021,** *155* (20), 204702.
38. Willets, K. A., Probing nanoscale interfaces with electrochemical surface-enhanced Raman scattering. *Curr Opin Electroche* **2019,** *13*, 18-24.
39. Wu, D. Y.; Li, J. F.; Ren, B.; Tian, Z. Q., Electrochemical surface-enhanced Raman spectroscopy of nanostructures. *Chem Soc Rev* **2008,** *37* (5), 1025-1041.
40. Tali, S. A. S.; Song, J.; Nam, W.; Zhou, W., Two-Tier Nanolaminate Plasmonic Crystals for Broadband Multiresonant Light Concentration with Spatial Mode Overlap. *Advanced Optical Materials* **2021,** *9* (10), 2001908.
41. Zhao, Y. M.; Xiao, C.; Mejia, E.; Garg, A.; Song, J. Y.; Agrawal, A.; Zhou, W., Voltage Modulation of Nanoplasmonic Metal Luminescence from Nano-Optoelectrodes in Electrolytes. *Acs Nano* **2023,** *17* (9), 8634-8645.
42. Xiao, C.; Zhao, Y.; Zhou, W., Nanoimprinted conducting nanopillar arrays made of MWCNT/polymer nanocomposites: a study by electrochemical impedance spectroscopy. *Nanoscale Advances* **2021,** *3* (2), 556-566.
43. Gui, J. Y.; Stern, D. A.; Frank, D. G.; Lu, F.; Zapien, D. C.; Hubbard, A. T., Adsorption and surface structural chemistry of thiophenol, benzyl mercaptan, and alkyl mercaptans. Comparative studies at silver (111) and platinum (111) electrodes by means of Auger spectroscopy, electron energy loss spectroscopy, low energy electron diffraction and electrochemistry. *Langmuir* **1991,** *7* (5), 955-963.
44. Zhong, C.-J.; Porter, M. D., Evidence for carbon-sulfur bond cleavage in spontaneously adsorbed organosulfide-based monolayers at gold. *Journal of the American chemical society* **1994,** *116* (25), 11616-11617.
45. Joo, T. H.; Kim, M. S.; Kim, K., Surface‐enhanced Raman scattering of benzenethiol in silver sol. *Journal of Raman spectroscopy* **1987,** *18* (1), 57-60.
46. Chuan Xiao, e., [Manuscript in preparation]. electrokinetic electrochemical surface enhanced raman spectroscopy. **2023**.
47. Mertens, J.; Kleemann, M.-E.; Chikkaraddy, R.; Narang, P.; Baumberg, J. J., How light is emitted by plasmonic metals. *Nano letters* **2017,** *17* (4), 2568-2574.
48. Nam, W.; Zhao, Y.; Song, J.; Ali Safiabadi Tali, S.; Kang, S.; Zhu, W.; Lezec, H. J.; Agrawal, A.; Vikesland, P. J.; Zhou, W., Plasmonic electronic raman scattering as internal standard for spatial and temporal calibration in quantitative surface-enhanced raman spectroscopy. *The journal of physical chemistry letters* **2020,** *11* (22), 9543-9551.
49. Carles, R.; Bayle, M.; Benzo, P.; Benassayag, G.; Bonafos, C.; Cacciato, G.; Privitera, V., Plasmon-resonant Raman spectroscopy in metallic nanoparticles: Surface-enhanced scattering by electronic excitations. *Physical Review B* **2015,** *92* (17), 174302.

50. Mooradian, A., Photoluminescence of metals. *Physical Review Letters* **1969,** *22* (5), 185.
51. Boyd, G.; Yu, Z.; Shen, Y., Photoinduced luminescence from the noble metals and its enhancement on roughened surfaces. *Physical Review B* **1986,** *33* (12), 7923.
52. Cai, Y.-Y.; Liu, J. G.; Tauzin, L. J.; Huang, D.; Sung, E.; Zhang, H.; Joplin, A.; Chang, W.-S.; Nordlander, P.; Link, S., Photoluminescence of gold nanorods: Purcell effect enhanced emission from hot carriers. *Acs Nano* **2018,** *12* (2), 976-985.
53. Lin, K.-Q.; Yi, J.; Hu, S.; Sun, J.-J.; Zheng, J.-T.; Wang, X.; Ren, B., Intraband hot-electron photoluminescence from single silver nanorods. *Acs Photonics* **2016,** *3* (7), 1248-1255.
54. Bates, R.; Macaskill, J., Standard potential of the silver-silver chloride electrode. *Pure Appl. Chem* **1978,** *50* (11-12), 1701-1706.
55. Liang, E. J.; Engert, C.; Kiefer, W., Surface-Enhanced Raman-Scattering of Halide-Ions, Pyridine and Crystal Violet on Colloidal Silver with near-Infrared Excitation - Low-Wave-Number Vibrational-Modes. *Vib Spectrosc* **1995,** *8* (3), 435-444.
56. Pargar, F.; Kolev, H.; Koleva, D. A.; van Breugel, K., Microstructure, surface chemistry and electrochemical response of Ag| AgCl sensors in alkaline media. *Journal of materials science* **2018,** *53* (10), 7527-7550.
57. Setiyanto, H.; Ferizal, M. Y. A.; Zulfikar, M. A.; Saraswaty, V.; Mufti, N. In *Modification of Carbon Paste Electrode with Molecularly Imprinted Poly (Gluthamic Acid) for Determination of Rhodamine: A Preliminary Study*, MSCEIS 2019: Proceedings of the 7th Mathematics, Science, and Computer Science Education International Seminar, MSCEIS 2019, 12 October 2019, Bandung, West Java, Indonesia, European Alliance for Innovation: 2020; p 474.
58. Zhao, Y.; Xiao, C.; Mejia, E.; Garg, A.; Song, J.; Agrawal, A.; Zhou, W., Voltage Modulation of Nanoplasmonic Metal Luminescence from Nano-Optoelectrodes in Electrolytes. *ACS nano* **2023**.
59. Croissant, J.; Zink, J. I., Nanovalve-controlled cargo release activated by plasmonic heating. *Journal of the American Chemical Society* **2012,** *134* (18), 7628-7631.
60. Baffou, G.; Polleux, J.; Rigneault, H.; Monneret, S., Super-heating and micro-bubble generation around plasmonic nanoparticles under cw illumination. *The Journal of Physical Chemistry C* **2014,** *118* (9), 4890-4898.
61. Burke, L. D.; Nugent, P. F., The Electrochemistry of Gold: I The Redox Behaviour of the Metal in Aqueous Media. *Gold Bulletin* **1997,** *30* (2), 43-53.
62. Freericks, J. K.; Devereaux, T. P., Raman scattering through a metal-insulator transition. *Physical Review B* **2001,** *64* (12), 125110.
63. Martina, I.; Wiesinger, R.; Jembrih-Simbürger, D.; Schreiner, M., Micro-Raman characterisation of silver corrosion products: instrumental set up and reference database. *E-Preserv Sci* **2012,** *9*, 1-8.
64. Chan, M. Y.; Leng, W.; Vikesland, P. J., Surface-Enhanced Raman Spectroscopy Characterization of Salt-Induced Aggregation of Gold Nanoparticles. *Chemphyschem* **2018,** *19* (1), 24-28.
65. Morales, D. M.; Risch, M., Seven steps to reliable cyclic voltammetry measurements for the determination of double layer capacitance. *J Phys-Energy* **2021,** *3* (3), 034013.
66. Bard, A., *Standard potentials in aqueous solution*. Routledge: 2017.
67. Aldous, L.; Silvester, D. S.; Villagrán, C.; Pitner, W. R.; Compton, R. G.; Lagunas, M. C.; Hardacre, C., Electrochemical studies of gold and chloride in ionic liquids. *New Journal of Chemistry* **2006,** *30* (11), 1576-1583.

68. Garrell, R. L.; Beer, K. D., Surface-enhanced Raman scattering from 4-ethylpyridine and poly (4-vinylpyridine) on gold and silver electrodes. *Langmuir* **1989,** *5* (2), 452-458.
69. Glaus, S.; Calzaferri, G., The band structures of the silver halides AgF, AgCl, and AgBr: A comparative study. *Photochemical & Photobiological Sciences* **2003,** *2*, 398-401.
70. Stefancu, A.; Lee, S.; Zhu, L.; Liu, M.; Lucacel, R. C.; Cortes, E.; Leopold, N., Fermi Level Equilibration at the Metal-Molecule Interface in Plasmonic Systems. *Nano Letters* **2021,** *21* (15), 6592-6599.
71. Huang, J.; Li, P.; Chen, S. L., Potential of zero charge and surface charging relation of metal-solution interphases from a constant-potential jellium-Poisson-Boltzmann model. *Physical Review B* **2020,** *101* (12), 125422.
72. Wakatsuki, T.; Furukawa, H.; Kawaguchi, K., Specific and non-specific adsorption of inorganic ions I. Evaluation of specific adsorbability by means of minimum concentration for specific adsorption. *Soil Science and Plant Nutrition* **1974,** *20* (4), 353-362.
73. Stefancu, A.; Lee, S.; Zhu, L.; Liu, M.; Lucacel, R. C.; Cortés, E.; Leopold, N., Fermi level equilibration at the metal–molecule interface in plasmonic systems. *Nano Letters* **2021,** *21* (15), 6592-6599.
74. Sigle, D. O.; Mertens, J.; Herrmann, L. O.; Bowman, R. W.; Ithurria, S.; Dubertret, B.; Shi, Y.; Yang, H. Y.; Tserkezis, C.; Aizpurua, J.; Baumberg, J. J., Monitoring morphological changes in 2D monolayer semiconductors using atom-thick plasmonic nanocavities. *Acs Nano* **2015,** *9* (1), 825-30.
75. Tazi, S.; Salanne, M.; Simon, C.; Tury, P.; Pounds, M.; Madden, P. A., Potential-Induced Ordering Transition of the Adsorbed Layer at the Ionic Liquid/Electrified Metal Interface. *J Phys Chem B* **2010,** *114* (25), 8453-8459.
76. Merlet, C.; Limmer, D. T.; Salanne, M.; van Roij, R.; Madden, P. A.; Chandler, D.; Rotenberg, B., The Electric Double Layer Has a Life of Its Own. *J Phys Chem C* **2014,** *118* (32), 18291-18298.
77. Novo, C.; Funston, A. M.; Gooding, A. K.; Mulvaney, P., Electrochemical charging of single gold nanorods. *J Am Chem Soc* **2009,** *131* (41), 14664-6.